

Carbon Monitoring System Flux Net Biosphere Exchange 2020 (CMS-Flux NBE 2020)

Junjie Liu^{1,2*}, Latha Baskaran¹, Kevin Bowman¹, David S. Schimel¹, A. Anthony Bloom¹, Nicholas C. Parazoo¹, Tomohiro Oda^{3,4}, Dustin Carroll⁵, Dimitris Menemenlis¹, Joanna Joiner⁶, Roisin Commane⁷, Bruce Daube⁸, Lucianna V. Gatti⁹, Kathryn McKain^{10,11}, John Miller¹⁰, Britton B. Stephens¹², Colm Sweeney¹⁰, Steven Wofsy⁸,

1. Jet Propulsion Laboratory, California Institute of Technology, CA
2. California Institute of Technology, CA
3. Global Modeling and Assimilation Office, NASA Goddard Space Flight Center
4. Goddard Earth Sciences Technology and Research, Universities Space Research Association, Columbia, MD
5. Moss Landing Marine Laboratories, San José State University, California, CA
6. Laboratory for Atmospheric Chemistry and Dynamics, NASA Goddard Space Flight Center
7. Lamont-Doherty Earth Observatory of Columbia University, NY
8. Harvard University, Cambridge, MA
9. LaGEE, CCST, INPE- National Institute for Space Research, Brazil
10. NOAA, Global Monitoring Laboratory, Boulder, CO 80305
11. University of Colorado, Cooperative Institute for Research in Environmental Sciences, Boulder, CO
11. National Center for Atmospheric Research, Boulder, CO 80301

Correspondence: Junjie Liu (junjie.liu@jpl.nasa.gov)
@ 2020 All rights reserved.

Abstract. Here we present a global and regionally-resolved terrestrial net biosphere exchange (NBE) dataset with corresponding uncertainties between 2010–2018: CMS-Flux NBE 2020. It is estimated using the NASA Carbon Monitoring System Flux (CMS-Flux) top-down flux inversion system that assimilates column CO₂ observations from the Greenhouse gases Observing SATellite (GOSAT) and NASA’s Observing Carbon Observatory -2 (OCO-2). The regional monthly fluxes are readily accessible as tabular files, and the gridded fluxes are available in NetCDF format. The fluxes and their uncertainties are evaluated by extensively comparing the posterior CO₂ mole fractions with CO₂ observations from aircraft and the NOAA marine boundary layer reference sites. We describe the characteristics of the dataset as global total, regional climatological mean, and regional annual fluxes and seasonal cycles. We find that the global total fluxes of the dataset agree with atmospheric CO₂ growth observed by the surface-observation network within uncertainty. Averaged between 2010 and 2018, the tropical regions range from close-to neutral in tropical South America to a net source in Africa; these contrast with the extra-tropics, which are a net sink of 2.5 ± 0.3 gigaton carbon per year. The regional satellite-constrained NBE estimates provide a unique perspective for understanding the terrestrial biosphere carbon dynamics and monitoring changes in regional contributions to the changes of atmospheric CO₂ growth rate. The gridded and regional aggregated dataset can be accessed at: <https://doi.org/10.25966/4v02-c391> (Liu et al., 2020).

47

48 **1 Introduction**

49 New “top-down” inversion frameworks that harness satellite observations provide an important
50 complement to global aggregated fluxes (e.g., Global Carbon Budget (GCB), Friedlingstein et al.,
51 2019) and inversions based on surface CO₂ observations (e.g., Chevallier et al., 2010), especially
52 over the tropics and the Southern Hemisphere (SH) where conventional surface CO₂ observations
53 are sparse. The net biosphere exchange (NBE), which is the net carbon flux of all the land-
54 atmosphere exchange processes except fossil fuel emissions, is far more variable and uncertainty
55 than ocean fluxes (Lovenduski and Bonan, 2017) or fossil fuel emissions (Yin et al, 2019), and is
56 thus the focus of this dataset estimated from a top-down atmospheric CO₂ inversion of satellite
57 column CO₂ dry-air mole fraction (X_{CO_2}). Here, we present the global and regional NBE as a series
58 of maps, time series and tables, and disseminate it as a public dataset for further analysis and
59 comparison to other sources of flux information. The gridded NBE dataset and its uncertainty, air-
60 sea fluxes, and fossil fuel emissions are also available, so that users can calculate carbon budget
61 from regional to global scale. Finally, we provide a comprehensive evaluation of both mean and
62 uncertainty estimates against the CO₂ observations from independent airborne datasets and the
63 NOAA marine boundary layer (MBL) reference sites (Conway et al., 1994).

64

65 Global top-down atmospheric CO₂ flux inversions have been historically used to estimate regional
66 terrestrial NBE. They make uses of the spatiotemporal variability of atmospheric CO₂, which is
67 dominated by NBE, to infer net carbon exchange at the surface (Chevallier et al., 2005; Baker et
68 al., 2006; Liu et al., 2014). The accuracy of the NBE from top-down flux inversions is determined

69 by the density and accuracy of the CO₂ observations, the accuracy of modeled atmospheric
70 transport, and knowledge of the prior uncertainties of the flux inventories.

71
72 For CO₂ flux inversions based on high precision *in situ* and flask observations, the measurement
73 error is low (<0.2 parts per million (ppm)) and not a significant source of error; however, these
74 observations are limited spatially, and are concentrating primarily over North America (NA) and
75 Europe (Crowell et al., 2019). Satellite X_{CO₂} from CO₂-dedicated satellites, such as the Greenhouse
76 Gases Observing Satellite (GOSAT) (launched in July 2009) and the Observing Carbon
77 Observatory 2 (OCO-2) (Crisp et al., 2017) have much broader spatial coverage (O'Dell et al.,
78 2018), which fill the observational gaps of conventional surface CO₂ observations, but they have
79 up to an order of magnitude higher single-sounding uncertainty and potential systematic errors
80 compared to the *in situ* and flask CO₂ observations. Recent progress in instrument error
81 characterization, spectroscopy, and retrieval methods have significantly improved the accuracy
82 and precision of the X_{CO₂} retrievals (O'Dell et al., 2018; Kiel et al., 2019). The single sounding
83 random error of X_{CO₂} from OCO-2 is ~1.0 ppm (Kulawik et al., 2019). A recent study by Byrne et
84 al. (2020) shows less than a 0.5 ppm difference between posterior X_{CO₂} constrained by a recent
85 data set, ACOS-GOSAT b7 X_{CO₂} retrievals, and those constrained by conventional surface CO₂
86 observations. Chevallier et al. (2019) also showed that an OCO-2 based flux inversion had similar
87 performance to surface CO₂ based flux inversions when comparing posterior CO₂ mole fractions
88 to aircraft CO₂ in the free troposphere. Results from these studies show that systematic
89 uncertainties in CO₂ retrievals from satellites are comparable to, or smaller than, other uncertainty
90 sources in atmospheric inversions (e.g. transport).

91

92 A newly-developed biogeochemical model-data fusion system, CARDAMOM, made progress in
93 producing NBE uncertainties, along with mean values that are consistent with a variety of
94 observations assimilated through a Markov Chain Monte Carlo (MCMC) method (Bloom et al.,
95 2016; 2020). Transport model errors in general have also been reduced relative to earlier transport
96 model intercomparison efforts, such as TransCom 3 (Gurney et al., 2004; Gaubert et al., 2019).
97 Advancements in satellite retrieval, transport, and prior terrestrial biosphere modeling have led to
98 more mature inversions constrained by satellite X_{CO_2} observations.

99

100 Two satellites, GOSAT and OCO-2, have now produced more than 10 years of observations. Here
101 we harness the CMS-Flux inversion framework (Liu et al., 2014; 2017; 2018; Bowman et al., 2017)
102 to generate an NBE product: CMS-Flux NBE 2020, by assimilating both GOSAT and OCO-2 from
103 2010–2018. The dataset is the longest satellite-constrained NBE product so far. The CMS-Flux
104 framework exploits globally available X_{CO_2} to infer spatially-resolved total surface-atmosphere
105 exchange. In combination with constituent fluxes, e.g., Gross Primary Production (GPP), NBE
106 from CMS-Flux framework have been used to assess the impacts of El Niño on terrestrial
107 biosphere fluxes (Bowman et al, 2017; Liu et al, 2017) and the role of droughts in the North
108 American carbon balance (Liu et al, 2018). These fluxes have furthermore been ingested into land-
109 surface data assimilation systems to quantify heterotrophic respiration (Konings et al., 2019),
110 evaluate structural and parametric uncertainty in carbon-climate models (Quetin et al., 2020), and
111 inform climate dynamics (Bloom et al., 2020). We present the regional NBE and its uncertainty
112 based on three types of regional masks: (1) latitude and continent, 2) distribution of biome types
113 (defined by plant functional types) and continent, and 3) TransCom regions (Gurney et al., 2004).

114

115 The outline of the paper is as follows: Section 2 describes methods, and Sections 3 and 4 describe
116 the dataset and the major NBE characteristics, respectively. We extensively evaluate the posterior
117 fluxes and uncertainties by comparing the posterior CO₂ mole fractions against aircraft
118 observations and the NOAA MBL reference CO₂, and a gross primary production (GPP) product
119 (section 5). In Section 6, we discuss the strength and weakness, and potential usage of the data. A
120 summary is provided in Section 7, and Section 8 describes the dataset availability and future plan.

121

122 **2 Methods**

123 **2.1 CMS-Flux inversion system**

124 The CMS-Flux framework is summarized in Figure 1. The center of the system is the CMS-Flux
125 inversion system, which optimizes NBE and air-sea net carbon exchanges with a 4D-Var inversion
126 system (Liu et al., 2014). In the current system, we assume no uncertainty in fossil fuel emissions,
127 which is a widely adopted assumption in global flux inversion systems (e.g., Crowell et al., 2019),
128 since the uncertainty in fossil fuel emissions at regional scales is substantially less than the NBE
129 uncertainties. The 4D-Var minimizes a cost function that includes two terms:

$$130 \quad J(\mathbf{x}) = (\mathbf{x} - \mathbf{x}_b)^T \mathbf{B}^{-1} (\mathbf{x} - \mathbf{x}_b) + (\mathbf{y} - h(\mathbf{x}))^T \mathbf{R}^{-1} (\mathbf{y} - h(\mathbf{x})) \quad (1)$$

131 The first term measures the differences between the optimized fluxes and the prior fluxes
132 normalized by the prior flux error covariance \mathbf{B} . The second term measures the differences between
133 observations (\mathbf{y}) and the corresponding model simulations ($h(\mathbf{x})$) normalized by the observation
134 error covariance \mathbf{R} . The term $h(\cdot)$ is the observation operator that calculates observation-
135 equivalent model-simulated X_{CO_2} . The 4D-Var uses the adjoint (i.e., the backward integration of
136 the transport model) (Henze et al., 2004) of the GEOS-Chem transport model to calculate the
137 sensitivity of the observations to surface fluxes. The configurations of the inversion system are

138 summarized in Table 1. We run both the forward and adjoint at $4^\circ \times 5^\circ$ spatial resolution, and
139 optimize monthly NBE and air-sea carbon fluxes at each grid point from January 2010 to
140 December 2018. Inputs for the system include prior carbon fluxes, meteorological drivers, and the
141 satellite X_{CO_2} (Figure 1). Section 2.2 (Table 2) describes the prior flux and its uncertainties, and
142 section 2.3 (Table 3) describes the observations and the corresponding uncertainties.

143

144 **2.2 The prior CO₂ fluxes and uncertainties**

145 The prior CO₂ fluxes include NBE, air-sea carbon exchange, and fossil fuel emissions (see Table
146 2). The data sources for the prior fluxes are listed in Table 7 and provided in the gridded fluxes.
147 Methods to generate prior ocean carbon fluxes and fossil fuel emissions are documented in Brix
148 et al., (2015), Carroll et al. (2020), and Oda et al. (2018). The focus of this dataset is optimized
149 terrestrial biosphere fluxes, so we briefly describe the prior terrestrial biosphere fluxes and their
150 uncertainties.

151

152 We construct the NBE prior using the CARDAMOM framework (Bloom et al., 2016). The
153 CARDAMOM data assimilation system explicitly represents the time-resolved uncertainties in the
154 NBE. The prior estimates are already constrained with multiple data streams accounting for
155 measurement uncertainties following a Bayesian approach similar to that used in the 4D-
156 variational approach. We use the CARDAMOM setup as described by Bloom et al. (2016, 2020)
157 resolved at monthly timescales; data constraints include GOME-2 solar-induced fluorescence
158 (Joiner et al., 2013), MODIS Leaf Area Index (LAI), and biomass and soil carbon (details on the
159 data assimilation are provided in Bloom et al. (2020)). In addition, mean GPP and fire carbon
160 emissions from 2010 - 2017 are constrained by FLUXCOM RS+METEO version 1 GPP

161 (Tramontana et al., 2016; Jung et al., 2017) and GFEDv4.1s (Randerson et al., 2018), respectively,
162 both assimilated with an uncertainty of 20%. We use the Olsen and Randerson (2001) approach to
163 downscale monthly GPP and respiration fluxes to 3-hourly timescales, based on ERA-interim re-
164 analysis of global radiation and surface temperature. Fire fluxes are downscaled using the
165 GFEDv4.1 daily and diurnal scale factors on monthly emissions (Giglio et al., 2013).
166 Posterior CARDAMOM NBE estimates are then summarized as NBE mean and standard
167 deviation values.

168

169 The NBE from CARDAMOM shows net carbon uptake of 2.3 GtC/year over the tropics and close
170 to neutral in the extratropics (Figure B1). The year-to-year variability (i.e., interannual variability,
171 IAV) estimated from CARDAMOM from 2010–2017 is generally less than 0.1 gC/m²/day outside
172 of the tropics (Figure B1). Because of the weak interannual variability estimated by CARDAMOM,
173 we use the same 2017 NBE prior for 2018.

174

175 CARDAMOM generates uncertainty along with the mean state. The relative uncertainty over the
176 tropics is generally larger than 100%, and the magnitude is between 50% and 100% over the extra-
177 tropics (Figure B2). We assume no correlation in the prior flux errors in either space or time. The
178 temporal and spatial error correlation estimates can in principle be computed by CARDAMOM.
179 We anticipate incorporating these error correlations in subsequent versions of this dataset.

180

181 **2.3 Column CO₂ observations from GOSAT and OCO-2**

182 We use the satellite-column CO₂ retrievals from Atmospheric Carbon Observations from Space
183 (ACOS) team for both GOSAT (version 7.3) and OCO-2 (version 9) (Table 3). The use of the
184 same retrieval algorithm and validation strategy adopted by the ACOS team to process both

185 GOSAT and OCO-2 spectra maximizes the consistency between these two datasets. Both GOSAT
186 and OCO-2 satellites carry high-resolution spectrometers optimized to return high precision
187 measurements of reflected sunlight within CO₂ and O₂ absorption bands in the shortwave infrared
188 (Crisp et al., 2012). Both satellites fly in a sun-synchronous orbit. GOSAT has a 13:00 ± 0.15
189 hours local passing time and a three-day ground track repeat cycle. The footprint of GOSAT is
190 ~10.5 km in diameter in sun-nadir view (Crisp et al., 2012). The daily number of soundings
191 processed by the ACOS-GOSAT retrieval algorithm is between a few hundreds to ~2000. Further
192 quality control and filtering reduce the ACOS-GOSAT X_{CO₂} retrievals to ~100 – 300 daily (Figure
193 B5 in Liu et al., 2017). We only assimilate ACOS-GOSAT land nadir observations flagged as
194 being good quality, which are the retrievals with quality flag equal to zero.

195
196 OCO-2 has a 13:30 local passing time and 16-day ground track repeat cycle. The nominal
197 footprints of the OCO-2 are 1.25 km wide and ~2.4 km along the orbit. Because of their small
198 footprints and sampling strategy, OCO-2 has many more X_{CO₂} retrievals than ACOS-GOSAT. To
199 reduce the sampling error due to the resolution differences between the transport model and OCO-
200 2 observations, we generate super observations by aggregating the observations within ~100 km
201 (along the same orbit) (Liu et al., 2017). The super-obsing strategy was first proposed in numerical
202 weather prediction (NWP) to assimilate dense observations (Lorenç, 1981), and is still broadly
203 used in NWP (e.g., Liu and Rabier, 2003). More detailed information about OCO-2 super
204 observations can be found in Liu et al. (2017). OCO-2 has four observing modes: land nadir, land
205 glint, ocean glint, and target. Following Liu et al. (2017), we only use land nadir observations. The
206 super observations have more uniform spatial coverage and are more comparable to the spatial

207 representation of ACOS-GOSAT observations and the transport model (see Figure B5 in Liu et
208 al., 2017).

209
210 We directly use observational uncertainty provided with ACOS-GOSAT b7.3 to represent the
211 observation error statistics, \mathbf{R} , in Eq 1. The uncertainty of the OCO-2 super observations is the
212 sum of the variability of X_{CO_2} used to generate each individual super observation and the mean
213 uncertainty provided in the original OCO-2 retrievals. Kulawik et al. (2019) showed that both
214 OCO-2 and ACOS-GOSAT bias-corrected retrievals have a mean bias of -0.1 ppm when compared
215 with X_{CO_2} from Total Carbon Column Observing Network (TCCON) (Wunch et al., 2011),
216 indicating consistency between ACOS-GOSAT and OCO-2 retrievals. O'Dell et al. (2018) showed
217 that the OCO-2 X_{CO_2} land nadir retrievals has RMS error of ~1.1 ppm when compared to TCCON
218 retrievals; the differences between OCO-2 X_{CO_2} retrievals and surface CO_2 constrained model
219 simulations are well within 1.0 ppm over most of the locations in the Northern Hemisphere (NH),
220 where most of the surface CO_2 observations are located.

221
222 The magnitude of observation errors used in \mathbf{R} is generally above 1.0 ppm, larger than the sum of
223 random error and biases in the observations. The ACOS-GOSAT b7.3 observations from July
224 2009–June 2015 are used to optimize fluxes between 2010 and 2014, and the OCO-2 X_{CO_2}
225 observations from Sep 2014–June 2019 are used to optimize fluxes between 2015 and 2018.

226
227 The observational coverage of ACOS-GOSAT and OCO-2 is spatiotemporally dependent, with
228 more coverage during summer than winter over the NH, and more observations over mid-latitudes
229 than over the tropics (Figure B3). The variability (i.e., standard deviation) of annual total number

230 of observations from 2010–2014 is within 4% of the annual mean number for ACOS-GOSAT.
231 Except for a data gap in 2017 caused by a malfunction of the OCO-2 instrument, the variability of
232 the annual total number of observations between 2015 and 2018 is within 8% of the annual mean
233 number for OCO-2.

234

235 **2.4 Uncertainty quantification**

236 The posterior flux error covariance is the inverse Hessian, which incorporates the transport,
237 measurement, and background errors at the 4D-Var solution (Eq. 13 in Bowman et al, 2017).
238 Posterior flux uncertainty projected to regions can be estimated analytically based on the methods
239 described in Fisher and Courtier (1995) and Meirink et al. (2008), using either flux singular vectors
240 or flux increments obtained during the iterative optimization (e.g., Niwa and Fujii, 2020). In this
241 study, we rely on a Monte Carlo approach to quantify posterior flux uncertainties following
242 Chevallier et al. (2010) and Liu et al. (2014), which is simpler and widely used. In this approach,
243 an ensemble of flux inversions is carried out with an ensemble of priors and simulated observations
244 to sample the uncertainties of prior fluxes (i.e., \mathbf{B} in eq. 1) and observations (\mathbf{R} in Eq. 1),
245 respectively. The magnitude of posterior flux uncertainties is a function of assumed uncertainties
246 in prior fluxes and observations, as well as the density of observations. Since the density of
247 GOSAT and OCO-2 observations are stable (section 2.3) within their respective data record, we
248 characterize the posterior flux uncertainties for 2010 and 2015 only, and assume the flux
249 uncertainties for 2011–2014 are the same as 2010 and flux uncertainties for 2016–2018 are the
250 same as 2015.

251

252 **2.5 Evaluation of posterior fluxes**

253 Direct NBE estimates from flux towers only provide a spatial representation of roughly 1 – 3
254 kilometers (Running et al., 1999), not appropriate to evaluate regional NBE from top-down flux
255 inversions. Thus, we use two methods to indirectly evaluate the posterior NBE and its uncertainties.
256 One is to compare annual NBE anomalies and seasonal cycle to a gross primary production (GPP)
257 product. The other is to compare posterior CO₂ mole fractions to independent (i.e., not assimilated
258 in the inversion) aircraft and the NOAA MBL reference observations. The second method has been
259 broadly used to indirectly evaluate posterior fluxes from top-down flux inversions (e.g., Stephens
260 et al., 2007; Liu and Bowman, 2016; Chevallier et al., 2019; Crowell et al., 2019). In addition to
261 these two methods, we also compare the NBE seasonal cycles to three publicly available top-down
262 NBE estimates that are constrained by surface CO₂ observations (Tables 3 and 7).

263 **2.5.1 Evaluation against independent gross primary production (GPP) product**

264 NBE is a small residual difference between two large terms: total ecosystem respiration (TER)
265 and GPP, plus fire. A positive NBE anomaly (i.e., less uptake from the atmosphere) has been
266 shown to correspond to reduced GPP caused by climate anomalies (e.g., Bastos et al., 2018), and
267 the magnitude of net uptake is proportional to GPP in most biomes observed by flux tower
268 observations (e.g., Falk et al., 2008). Since NBE is related not only to GPP, the comparison to GPP
269 only serves as a qualitative measure of the NBE quality. For example, we would expect that the
270 posterior NBE seasonality to be anti-correlated with GPP in the temperate and high latitudes. In
271 this study, we use FLUXSAT GPP (Joiner et al., 2018), which is an upscaled GPP product based
272 on flux tower GPP observations and satellite-based geometry adjusted reflectance from the
273 MODerate-resolution Imaging Spectroradiometer (MODIS) and solar-induced chlorophyll
274 fluorescence observations from Global Ozone Monitoring Experiment – 2 (GOME-2) (Joiner et

275 al., 2013). Joiner et al. (2018) show that the agreement between FLUXSAT-GPP and GPP from
276 flux towers is better than other available upscaled GPP products.

277 **2.5.2 Evaluation against aircraft and the NOAA marine boundary layer (MBL)** 278 **reference CO₂ observations**

279 The aircraft observations used in this study include those published in OCO-2 MIP ObsPack
280 August 2019 (CarbonTracker team, 2019), which include regular vertical profiles from flask
281 samples collected on light aircraft by NOAA (Sweeney et al., 2015) and other laboratories, regular
282 (two to four weekly) vertical profiles from the Instituto de Pesquisas Espaciais (INPE) over
283 tropical South America (SA) (Gatti et al., 2014), and from the Atmospheric Tomography (ATom,
284 Wofsy et al., 2018), HIAPER Pole-to-Pole (HIPPO, Wofsy et al., 2011), the O₂/N₂ Ratio and CO₂
285 airborne Southern Ocean Study (ORCAS) (Stephens et al., 2017), and Atmospheric Carbon and
286 Transport - America (ACT-America, Davis et al., 2018) aircraft campaigns (Table 3). Figure 2
287 shows the aircraft observation coverage and density between 2010 and 2018. Most of the aircraft
288 observations are concentrated over NA. ATom had four (1–4) campaigns between August 2016 to
289 May 2018, spanning four seasons over the Pacific and Atlantic Ocean. HIPPO had five (1–5)
290 campaigns over the Pacific, but only HIPPO 3–5 occurred between 2010 and 2011. HIPPO 1–2
291 occurred in 2009. Based on the spatial distribution of aircraft observations, we divide the
292 comparison into nine regions: Alaska, mid-latitude NA, Europe, East Asia, South Asia, Africa,
293 Australia, Southern Ocean, and South America (Table 4 and Figure 2).

294
295 We calculate several quantities to evaluate the posterior fluxes and their uncertainty with aircraft
296 observations. One is the monthly mean differences between posterior and aircraft CO₂ mole

297 fractions. The second is the monthly root mean square errors (RMSE) over each of nine sub-
 298 regions, which is defined as:

$$299 \quad RMSE = \left(\frac{1}{n} \sum_{i=1}^n (y_{aircraft}^o - y_{aircraft}^b)_i \right)^{\frac{1}{2}} \quad (2)$$

300 where $y_{aircraft}^o$ is the i^{th} aircraft observation, $y_{aircraft}^b$ is the corresponding posterior CO₂ mole
 301 fraction sampled at the i^{th} aircraft location, and n is the number of aircraft observations over each
 302 region. The RMSE is computed over the n aircraft observations within one of the nine sub-regions.
 303 The mean differences indicate the magnitude of the mean posterior CO₂ bias, while the RMSE
 304 includes both random and systematic errors in posterior CO₂. The bias and RMSE could be due to
 305 errors in posterior fluxes, transport, and initial CO₂ concentrations. When errors in transport and
 306 initial CO₂ concentrations are smaller than the errors in the posterior fluxes, the magnitude of
 307 biases and *RMSE* indicates the accuracy of the posterior fluxes.

308
 309 To evaluate the magnitude of posterior flux uncertainty estimates, we compare *RMSE* against the
 310 standard deviation of ensemble simulated aircraft observations (equation 3) from the Monte Carlo
 311 method (*RMSE_{MC}*). The quantity *RMSE_{MC}* can be written as:

$$312 \quad RMSE_{MC} = \left[\frac{1}{nens} \sum_{iens=1}^{nens} ((y_{aircraft}^{b(MC)})_{iens} - \bar{y}_{aircraft}^{b(MC)})^2 \right]^{\frac{1}{2}} \quad (3)$$

313 The variable $(y_{aircraft}^{b(MC)})_{iens}$ is the i^{th} ensemble member of simulated aircraft observations from
 314 Monte Carlo ensemble simulations, $\bar{y}_{aircraft}^{b(MC)}$ is the mean, and *nens* is the total number of ensemble
 315 members. For simplicity, in equation (3), we drop the indices for the aircraft observations used in
 316 equation (2). In the absence of errors in transport and initial CO₂ concentrations, when the
 317 estimated posterior flux uncertainty reflects the “true” posterior flux uncertainty, we show in the
 318 *Appendix* that:

319 $RMSE^2 = \frac{1}{n} \sum_{i=1}^n R_{i,i} + RMSE_{MC}^2$ (4)

320 where $R_{aircraft}$ is the aircraft observation error variance, which could be neglected on regional
321 scale.

322

323 We further calculate the ratio r between $RMSE$ and $RMSE_{MC}$:

324 $r = \frac{RMSE}{RMSE_{MC}}$ (5)

325 A ratio close to one indicates that the posterior flux uncertainty reflects the true uncertainty in the
326 posterior fluxes when the transport errors are small.

327

328 The presence of transport errors will make the comparison between $RMSE$ and $RMSE_{MC}$
329 potentially difficult to interpret. Even when $RMSE_{MC}$ represents the actual uncertainty in posterior
330 fluxes, the $RMSE$ could be larger than $RMSE_{MC}$, since the differences between aircraft
331 observations and model simulated posterior mole fractions $RMSE$ could be due to errors in both
332 transport and the posterior fluxes, while $RMSE_{MC}$ only reflects the impact of posterior flux
333 uncertainty on simulated aircraft observations. In this study, we assume the primary sources of
334 $RMSE$ come from errors in posterior fluxes.

335

336 The $RMSE$ and $RMSE_{MC}$ comparison only shows differences in CO_2 space. We further calculate
337 the sensitivity of the $RMSE$ to the posterior flux using the GEOS-Chem adjoint. We first define a
338 cost function J as:

339 $J = RMSE^2$ (6)

340 The sensitivity of the mean-square error to a flux, x , at location i and month j is

341 $w_{i,j} = \frac{\partial J}{\partial x_{i,j}} \times x_{i,j}$ (7)

342 This sensitivity is normalized by the flux magnitude. Equation 7 can be interpreted as the
343 sensitivity of the $RMSE^2$ to a fractional change in the fluxes. We can estimate the time-integrated
344 magnitude of the sensitivity over the entire assimilation window by calculating:

345 $S_i = \frac{\sum_{j=1}^M |w_{i,j}|}{\sum_{k=1}^P \sum_{j=1}^M |w_{k,j}|}$ (8)

346 where P is the total number of grid points and M is the total number of months from the time of
347 the aircraft data to the beginning of the inversion. The numerator of equation (8) quantifies the
348 absolute total sensitivity of the $RMSE^2$ to the fluxes at the i^{th} grid. Normalized by the total absolute
349 sensitivity across the globe, the quantity S_i indicates the relative sensitivity of $RMSE^2$ to fluxes at
350 the i^{th} grid point. Note that S_i is unitless, and it only quantifies sensitivity, not the contribution of
351 fluxes at each grid to $RMSE^2$.

352

353 We use the NOAA MBL reference dataset (Table 7) to evaluate the CO_2 seasonal cycle over four
354 latitude bands: 90°N-60°N, 60°N-20°N, 20°N-20°S, and 20°S-90°S. The MBL reference is based
355 on a subset of sites from the NOAA Cooperative Global Air Sampling Network. Only
356 measurements that are representative of a large volume air over a broad region are considered. In
357 the comparison, we first remove the global mean CO_2
358 (<https://www.esrl.noaa.gov/gmd/ccgg/trends/global.html>) from both the NOAA MBL reference
359 and the posterior CO_2 .

360

361 **2.6 Regional masks**

362 We provide posterior NBE from 2010 – 2018 using three sets of regional masks (Figure 3), in
363 addition to the gridded product. The regional mask in Figure 3A is based on a combination of
364 seven plant function types condensed from MODIS IGBP and the TransCom -3 regions (Gurney
365 et al., 2004), which is referred as Region Mask 1 (RM1) in later description. There are 28 regions
366 in Figure 3A: six in NA, four in SA, five in Eurasia (north of 40°N), three in tropical Asia, three
367 in Australia, and seven in Africa. The regional mask in Figure 3B is based on latitude and
368 continents with 13 regions in total, which is referred as Region Mask 2 (RM2) in later description.
369 Figure 3C is the TransCom regional mask with 11 regions on land.

370

371 **3 Dataset description**

372

373 We present the fluxes as globally, latitudinally, and regionally aggregated time series. We show
374 the nine-year average fluxes aggregated into RM1, RM2, and TransCom regions (Figure 3). The
375 aggregations are geographic (latitude and continent) and bio-climatic (biome by continent). For
376 each region in the geographic and biome aggregations, we show nine-year mean annual net fluxes
377 and uncertainties, and then the annual fluxes for each region as a set of time-series plots. The
378 month-by-month fluxes and uncertainties are available in tabular format, so the actual aggregated
379 fluxes may be readily compared to bottom-up extrapolated fluxes and Earth System models. Users
380 can also aggregate the gridded fluxes and uncertainties based on their own defined regional masks.
381 Table 5 provides a complete list of all data products available in the dataset. In section 4, we
382 describe the major characteristics of the dataset.

383 **4 Characteristics of the dataset**

384 **4.1 Global fluxes**

385 The annual atmospheric CO₂ growth rate, which is the net difference between fossil fuel emissions
386 and total annual sink over land and ocean, is well-observed by the NOAA surface CO₂ observing
387 network (<https://www.esrl.noaa.gov/gmd/ccgg/ggrn.php>). We compare the global total flux estimates
388 constrained by GOSAT and OCO-2 with the NOAA CO₂ growth rate from 2010–2018, and discuss
389 the mean carbon sink over land and ocean. Over these nine years, the satellite-constrained
390 atmospheric CO₂ growth rate agrees with the NOAA observed CO₂ growth rate within the
391 uncertainty of the posterior fluxes (Figure 4). The mean annual global surface CO₂ fluxes (in Gt
392 C/yr) are derived from the NOAA observed CO₂ growth rate (in ppm/yr) using a conversion factor
393 of 2.124 GtC/ppm (Le Quéré et al., 2018). The estimated growth rate has the largest discrepancy
394 with the NOAA observed growth rate in 2014, which may be due to a failure of one of the two
395 solar paddles of GOSAT in May 2014 (Kuze et al., 2016). Over the nine years, the estimated total
396 accumulated carbon in the atmosphere is 41.5 ± 2.4 GtC, which is slightly lower than the
397 accumulated carbon based on the NOAA CO₂ growth rate (45.2 ± 0.4 GtC). On average, we
398 estimate that the NBE is 2.0 ± 0.7 GtC, $\sim 20 \pm 8\%$ of fossil fuel emissions, and the ocean sink is
399 3.0 ± 0.1 GtC, $\sim 30 \pm 1\%$ of fossil fuel emissions (Figure 4). These numbers are within the ranges
400 of the corresponding GCB estimates from Freidlingstein et al., 2019 (referred as GCB-2019
401 hereafter). The mean NBE and ocean sink from GCB-2019 are 2.0 ± 1.0 GtC and 2.5 ± 0.5 GtC
402 respectively, which are $21 \pm 10\%$ and $26 \pm 5\%$ of fossil fuel emissions respectively between 2010–
403 2018. The GCB does not report NBE directly, we calculate NBE from GCB-2019 as the residual
404 differences between fossil fuel, ocean net carbon sink, and atmospheric CO₂ growth rate. It is also
405 equivalent to $(S_{\text{LAND}} + B_{\text{IM}} - E_{\text{LUC}})$ reported by Freidlingstein et al., 2019, where S_{LAND} is terrestrial
406 sink, B_{IM} is a budget imbalance, and E_{LUC} is land use change. Over these nine years, we estimate
407 that NBE ranges from 3.6 GtC ($\sim 37\%$ of fossil fuel emissions) in 2011 (a La Niña year), to only

408 0.5 GtC, (~5% of fossil fuel emissions) in 2015 (an El Niño year), consistent with 3.3 GtC (35%
409 of fossil fuel) in 2011 to 0.9 GtC (7% of fossil fuel) in 2015 estimated from GCB-2019. We
410 estimate that the ocean sinks range from 3.5 GtC in 2015 to 2.3 GtC in 2012, larger than the
411 estimated ocean flux ranges of 2.7 in 2016 to 2.5 in 2012 reported by Freidlingstein et al. (2019).

412 **4.2 Mean regional fluxes and uncertainties**

413 Figure 5 shows the nine-year mean regional annual fluxes, uncertainty, and its variability between
414 2010–2018. Table 6 shows an example of the dataset corresponding to Figure 5 A, D, and G. It
415 shows that large net carbon uptake occurs over Eurasia, NA, and the Southern Hemisphere (SH)
416 mid-latitudes. The largest net carbon uptake is over the eastern US (-0.4 ± 0.1 GtC (1σ uncertainty))
417 and high latitude Eurasia (-0.5 ± 0.1 GtC) (Figure 5A, B). We estimate a net land carbon sink of
418 2.5 ± 0.3 GtC/year between 2010–2013 over the NH mid to high latitudes, which agrees with 2.4
419 ± 0.6 GtC estimates over the same time periods based on a two-box model (Ciais et al., 2019). Net
420 uptake in the tropics ranges from close-to-neutral in tropical South America (0.1 ± 0.1 GtC) to a
421 net source in northern Africa (0.6 ± 0.2 GtC) (Figure 5A, B). The tropics exhibit both large
422 uncertainty and large variability. The NBE interannual variability over northern Africa and tropical
423 SA are 0.5 GtC and 0.3 GtC respectively, larger than the 0.2 GtC and 0.1 GtC uncertainty (Figure
424 5D, E). We also find collocation of regions with large NBE and FLUXSAT-GPP interannual
425 variability (Figure B4). The availability of flux estimates over the broadly used TransCom regions
426 make it easy to compare to previous studies. For example, we estimate that the annual net carbon
427 uptake over North America is 0.7 ± 0.1 GtC/year with 0.2 GtC variability between 2010 and 2018,
428 which agrees with 0.7 ± 0.5 GtC/year estimates based on surface CO₂ observations between 1996-
429 2007 (Peylin et al., 2013).

430

431 **4.3 Interannual variabilities and uncertainties**

432 Here we present hemispheric and regional NBE interannual variabilities and corresponding
433 uncertainties (Figures 6 and 7, and corresponding tabular data files). In Figure 6, we further divide
434 the globe into three large latitude bands: tropics (20°S–20°N), NH extra-tropics (20°N–85°N), and
435 SH extra-tropics (60°S–20°S). The tropical NBE contributes 90% to the global NBE interannual
436 variability (IAV). The IAV of NBE over the extra-tropics is only about one-third of that over the
437 tropics. The dominant role of tropical NBE in the global IAV of NBE agrees with Figure 4 in
438 Sellers et al. (2018). The top-down global annual NBE anomaly is within the 1.0 GtC/yr
439 uncertainty of residual NBE (i.e., fossil fuel – atmospheric growth – ocean sink) calculated from
440 GCB-2019 (Friedlinston et al., 2019) (Figure 6).

441
442 Figure 7 shows the annual NBE anomalies and uncertainties over a few selected regions based on
443 RM1. Positive NBE indicates reduced net uptake relative to the 2010–2018 mean, and vice versa.
444 Also shown in Figure 7 are GPP anomalies estimated from FLUXSAT. Positive GPP indicates
445 increased productivity, and vice versa. GPP drives NBE in years where anomalies are inversely
446 correlated (e.g., positive NBE and negative GPP), and TER drives NBE in years where anomalies
447 of GPP and NBE have the same sign or are weakly correlated. Over tropical SA evergreen
448 broadleaf forest, the largest positive NBE anomalies occur during the 2015–2016 El Niño,
449 corresponding to large reductions in productivity, consistent with Liu et al. (2017). In 2017, the
450 region sees increased net uptake and increased productivity, implying a recovery from the 2015–
451 2016 El Niño event. The variability in GPP explains 80% of NBE variability over this region over
452 the nine-year period. In Australian shrubland, our inversion captures the increased net uptake in
453 2010 and 2011 due to increased precipitation (Poulter et al., 2014) and increased productivity. The

454 variability in GPP explains 70% of the interannual variability in NBE. Over tropical south America
455 savanna, the NBE interannual variability also shows strong negative correlations with GPP, with
456 GPP explaining 40% of NBE interannual variability. Over the mid-latitude regions where the IAV
457 is small, the R^2 between GPP and NBE is also small (0.0–0.5) as expected. But the increased net
458 uptake generally corresponds to increased productivity. We also do not expect perfect negative
459 correlation between NBE anomalies and GPP anomalies, as discussed in section 2.5. The
460 comparison between NBE and GPP provides insight into when and where net fluxes are likely
461 dominated by productivity.

462

463 **4.4 Seasonal cycle**

464 We provide the regional mean NBE seasonal cycle, its variability, and uncertainty based on the
465 three regional masks (Table 5). Here we briefly describe the characteristics of the NBE seasonal
466 cycle over the 11 TransCom regions, and its comparison to three independent top-down inversion
467 results based on surface CO_2 , which are CT-Europe (e.g., van der Laan-Luijkx et al., 2017) CAMS
468 (Chevallier et al., 2005), and Jena CarbonScope (Rödenbeck et al., 2003). CMS-Flux-NBE differs the
469 most from surface- CO_2 based inversions over the South American Tropical, Northern Africa,
470 tropical Asia, and NH boreal regions. The CMS-Flux NBE has a larger seasonal cycle amplitude
471 over tropical Asia and Northern Africa, where the surface CO_2 constraint is weak, while it has a
472 smaller seasonal cycle amplitude over the boreal region; this may be due to the sparse satellite
473 observations over the high latitudes and weaker seasonal amplitude of the prior CARDAMOM
474 fluxes. The comparison to FluxSat GPP can only qualitatively evaluate the NBE seasonal cycle,
475 but cannot differentiate among different estimates. In general, the months that have larger
476 productivity corresponds to months with a net uptake of carbon from the atmosphere, especially

477 over the NH (Figure 8). More research is still needed to understand the seasonal cycles of NBE,
478 including its phase (i.e., transition from source to sink) and amplitude (peak-to-trough difference),
479 and its relationships with GPP and respiration.

480

481 **5 Evaluation against independent aircraft CO₂ observations**

482 **5.1 Comparison to aircraft observations over nine sub-regions**

483 In this section, we evaluate posterior CO₂ against aircraft observations over the nine sub-regions
484 listed in Table 4 and Figure 2. We compare the posterior CO₂ to aircraft CO₂ mole fractions above
485 the planetary boundary layer and up to mid troposphere (1–5 km) at the locations and time of
486 aircraft observations, and then calculate the monthly mean error statistics between 1–5 km. The
487 aircraft observations between 1–5 km are more sensitive to regional fluxes (Liu et al., 2015; Liu
488 and Bowman, 2016). Scatter plots in the left column of Figure 9 show regional monthly mean de-
489 trended aircraft CO₂ observations (x-axis) versus the simulated detrended posterior CO₂ (y-axis).
490 We used the NOAA global CO₂ trend to detrend both the observations and model simulated mole
491 fractions (ftp://aftp.cmdl.noaa.gov/products/trends/co2/co2_trend_gl.txt). Over the NH regions (A,
492 B, C, D) and Africa (F), the R² is greater than or equal to 0.9, which indicates that the posterior
493 CO₂ captures the observed seasonality. The low R² (0.7) value in South Asia is caused by one
494 outlier. Over the Southern Ocean, Australia, and SA, the R² is between 0.2 and 0.4, reflecting
495 weaker CO₂ seasonality over these regions and possible bias in ocean flux estimates (see
496 discussions later).

497

498 The right panel of Figure 9 shows the monthly mean differences between posterior CO₂ and aircraft
499 observations (black), *RMSE* (equation 2) (blue line), and *RMSE_{MC}* (equation 3) (red line). The

500 magnitude of the mean differences between the posterior CO₂ and aircraft observations is less than
501 0.5 ppm except over the Southern Ocean, which has a -0.8 ppm bias. The mean differences between
502 posterior CO₂ and aircraft observations are primarily caused by errors in transport and biases in
503 assimilated satellite observations, while $RMSE_{MC}$ is ‘internal flux error’ projected into mole
504 fraction space. With the exception of the Southern Ocean, for all regions mean bias is significantly
505 less than $RMSE_{MC}$, which suggests that transport and data bias in satellite observations may be
506 much smaller than the internal flux errors. Note that $RMSE_{MC}$ is smaller than $RMSE$ over the first
507 ~six months of simulation, which may indicate a dominant impact of errors in transport and initial
508 CO₂ concentration on posterior CO₂ $RMSE$.

509

510 As demonstrated in section 2.5, comparing $RMSE$ and $RMSE_{MC}$ is a test of the accuracy of posterior
511 flux uncertainty estimate. Over all the regions, the differences between $RMSE$ and $RMSE_{MC}$ are
512 smaller than 0.3 ppm, which indicates a comparable magnitude between empirical posterior flux
513 uncertainty estimates from the Monte Carlo method and the actual posterior flux uncertainty over
514 the regions that these aircraft observations are sensitive to. These aircraft observations are sensitive
515 to NBE over a broad region as shown in Figure B5. Note, Figure B5 and Figures B8-B10 are
516 calculated using equation (8).

517

518 **5.2 Comparison to aircraft observations from ATom and HIPPO aircraft campaigns**

519 Figures 10 and 11 show comparisons to aircraft CO₂ from ATom 1–4 campaigns spanning four
520 seasons, and HIPPO 3–5 over the Pacific Ocean between 1–5 km. The vertical curtain comparisons
521 are shown in Figure B6 and B7. The mean differences between posterior CO₂ and aircraft CO₂ are
522 quite uniform (within 0.5 ppm) throughout the column except over the Atlantic Ocean during

523 ATom 1–2 and the Southern Ocean during ATom 1 (Figures S6 and S7). Also shown in Figures
524 10 and 11 are $RMSE$ of each aircraft campaign (middle column) and the ratio between $RMSE$ and
525 $RMSE_{MC}$ (right column). A ratio larger than one between $RMSE$ and $RMSE_{MC}$ indicates errors in
526 either transport or underestimation of the posterior flux uncertainty (section 2.5).

527

528 Over most of the flight tracks during ATom 1–4, the posterior CO_2 errors are between -0.5 and 0.5
529 ppm, the $RMSE$ is smaller than 0.5 ppm, and the ratio between $RMSE$ and $RMSE_{MC}$ is smaller than
530 or equal to 1. However, off the coast of Africa during ATOM -1 and -2 and over the Southern
531 Ocean during ATOM-1, the mean differences between posterior CO_2 and aircraft observations are
532 larger than 0.5 ppm. During ATOM-1 (29 July – 23 Aug 2016), the mean differences between
533 posterior CO_2 and aircraft CO_2 show large negative biases, while during ATOM-2 (26 Jan 2017–
534 21 Feb 2017), it has large positive biases off the coast of Africa. The ratio between $RMSE$ and
535 $RMSE_{MC}$ is significantly larger than one over these regions, which indicates an underestimation of
536 posterior flux uncertainty or large magnitude of transport errors during that time period.

537

538 We further run adjoint sensitivity analyses over the three regions with ratios significantly larger
539 than one to identify the posterior fluxes that could contribute to the large differences between
540 posterior CO_2 and aircraft observations during ATOM 1–2. We run the adjoint model backward
541 for three months from the observation time and calculate S_i as defined in equation (7). The adjoint
542 sensitivity analysis indicates that the large mismatch between aircraft observations and model
543 simulations during ATOM-1 and -2 off the coast of Africa could be potentially driven by errors in
544 posterior fluxes over tropical Africa (Figure B8). The large posterior CO_2 errors and large ratio
545 between $RMSE$ and $RMSE_{MC}$ over the Southern Ocean during ATOM-1 are driven by flux errors

546 in oceanic fluxes around 30°S and over Australia (Figure B9), which also contribute to the large
547 errors in comparison to aircraft observations over the Southern Ocean shown in Figure 9 H.

548

549 During the HIPPO aircraft campaigns, the absolute errors in posterior CO₂ across the Pacific are
550 less than 0.5 ppm except over the Arctic Ocean and over Alaska in summer (Figure 11), consistent
551 with Figure 10A. The large errors over the Arctic Ocean may be related to both transport errors
552 and the accuracy of high latitude fluxes. Byrne et al. (2020) provide a brief summary of the
553 challenges in simulating CO₂ over high latitudes using a transport model with 4° x 5° resolution.
554 Increasing the resolution of the transport model may reduce transport errors over high latitudes.

555

556 We run adjoint sensitivity analysis over the high-latitude regions where the differences between
557 posterior CO₂ and aircraft observations are large (Figure 11). The adjoint sensitivity analysis
558 (Figure B10) shows that the large errors over these regions could be driven by errors in fluxes over
559 Alaska as well as broad NH mid-latitude regions.

560

561 **5.3 Comparison to MBL reference sites**

562 Since MBL reference sites sample air over broad regions, the comparison to detrended MBL
563 observations indirectly evaluates the NBE over large regions. Figure 12 shows the comparison
564 over four latitude bands. The uncertainty of posterior CO₂ concentration is from the MC method.
565 Except over 90°S-20°S, the differences between observations and posterior CO₂ are within
566 posterior CO₂ uncertainty estimates. The posterior CO₂ concentrations have the smallest bias and
567 random errors over the tropical latitude band. The R² is above 0.9 over NH mid to high latitudes,
568 consistent with Figure 9. Over 90°S-20°S, the posterior CO₂ has positive bias in 2013 and 2014

569 and negative bias and much weaker seasonality between Jan 2015 – Dec 2018 compared to
570 observations, which indicates possible biases in Southern Ocean flux estimates (Figure B11). The
571 low bias over the Southern Ocean is consistent with aircraft comparison during OCO-2 period
572 (Figures 9-10, Figure B9). The changes of performance after 2013 over 90°S-20°S is most likely
573 due to the prior ocean carbon fluxes. Evaluation of ocean carbon fluxes is out of scope of this study.
574 Note, since we only assimilate land-nadir X_{CO_2} observations in this study due to known issues with
575 the OCO-2 v9 ocean glint observations (O'Dell et al., 2018), the constraint of top-down inversion
576 on air-sea CO_2 exchanges is weak (not shown). The ocean glint observations of OCO-2 v10
577 observations have been improved compared to v9 (Osterman et al., 2020). We expect to have better
578 estimate of ocean carbon fluxes over the Southern Ocean when assimilating both land and ocean
579 X_{CO_2} observations from GOSAT and OCO-2 in the future.

580 581 **6 Discussion**

582 Evaluation of posterior flux uncertainty estimates by comparing posterior CO_2 error statistics
583 ($RMSE$, Equation 2) with the standard deviation of ensemble simulated CO_2 from Monte Carlo
584 uncertainty quantification method ($RMSE_{MC}$, equation 3) has its limitations. A comparable $RMSE$
585 and $RMSE_{MC}$ indicates a small magnitude of transport errors and reasonable posterior uncertainty
586 estimates. A much larger $RMSE$ than $RMSE_{MC}$ could be due to errors in either transport or
587 underestimation of the posterior flux uncertainty or both. The presence of transport errors makes
588 the interpretation of the $RMSE$ and $RMSE_{MC}$ complex. A better, independent quantification of
589 transport errors is needed in the future in order to rigorously use the comparison statistics between
590 aircraft observations and posterior CO_2 to diagnose flux errors.

591

592 Comparison to aircraft observations shows regionally-dependent accuracy in posterior fluxes.
593 ATom observations show seasonally-dependent biases over the Atlantic, implying possible
594 seasonally dependent errors in posterior fluxes over northern to central Africa. Therefore, we
595 recommend combining NBE with other ancillary variables, e.g., GPP, to better understand carbon
596 dynamics. Combining NBE with component carbon fluxes can shed light on the processes
597 controlling the changes of NBE (e.g., Bowman et al, 2017; Liu et al., 2017). NBE can be written
598 as:

$$599 \text{NBE} = \text{TER} + \text{fire} - \text{GPP} \quad (8)$$

600 where TER is total ecosystem respiration (TER) (Figure 1). Satellite carbon monoxide (CO)
601 observations provide constraints on fire emissions (Arellano et al, 2006, van der Werf, 2008; Jones
602 et al, 2009; Jiang et al., 2015, Bowman et al, 2017; Liu et al., 2017). In addition to the FLUXSAT-
603 GPP product used here, solar induced chlorophyll fluorescence (SIF) can be directly used as a
604 proxy for GPP (e.g., Parazoo et al, 2014). Once NBE, fire, and GPP carbon fluxes are quantified,
605 TER can be calculated as a residual (e.g., Bowman et al, 2017; Liu et al., 2017, 2018).

606

607 Because of the diffusive manner of atmospheric transport and the limited observation coverage,
608 the gridded flux values are not independent from each other. The errors and uncertainties of the
609 fluxes at each individual grid point are larger than regional aggregated fluxes. Interpreting NBE at
610 each individual grid point requires caution. But at the same time, satellite CO₂ constrained NBE
611 can potentially resolve fluxes at spatial scales smaller than the traditional TransCom regions. Here,
612 we provide regional fluxes at two predefined regions in addition to TransCom. We encourage data
613 users to use the data at appropriate regional scales.

614

615 The variability and changes are more robust than the mean NBE fluxes from top-down flux
616 inversions in general (Baker et al., 2006b). The errors in transport and potential biases in
617 observations are mostly stable in time, so biases in the mean fluxes tend to cancel out when
618 computing interannual variability and year-to-year changes (Schuh et al., 2019; Crowell et al.,
619 2019).

620
621 The global fossil fuel emissions have ~5% uncertainty (GCB-2019). However, they are regionally
622 inhomogeneous. We neglect the uncertainties in fossil fuel emissions, which will introduce
623 additional error in regions of rapid fossil fuel growth or in areas with noisier statistics (Yin et al.,
624 2019). In the future, we will account for uncertainties in fossil fuel emissions.

625
626 The posterior NBE includes all types of land fluxes except fossil fuel emissions, which is
627 equivalent to the sum of land use change fluxes, land sinks, and residual imbalance published by
628 the GCB-2019. The sum of regional NBE and fossil fuel emissions is an index of the contribution
629 of any specific region to the changes of the atmospheric CO₂ growth rate. Since the predicted
630 changes of NBE in the future have large uncertainties (Lovenduski and Bonan, 2017), quantifying
631 regional NBE is critical to monitoring regional contributions to atmospheric CO₂ growth rate, and
632 ultimately to guide mitigation to limit warming to 1.5°C above pre-industrial levels (IPCC, 2018).

633

634 **7 Summary**

635 Terrestrial biosphere carbon fluxes are the largest contributor to the interannual variability of the
636 atmospheric CO₂ growth rate. Therefore, monitoring its change at regional scales is essential for
637 understanding how it responds to CO₂, climate and land use. Here, we present the longest terrestrial

638 flux estimates and their uncertainties constrained by X_{CO_2} from 2010–2018 on self-consistent
639 global and regional scales (CMS-Flux NBE 2020). We qualitatively evaluate the NBE estimates
640 by comparing its variability with GPP variability, and provide comprehensive evaluation of
641 posterior fluxes and the uncertainties by comparing posterior CO_2 with independent CO_2
642 observations from aircraft and the NOAA MBL reference sites. This dataset can be used in
643 understanding controls on regional NBE interannual variability, evaluating biogeochemical
644 models, and supporting the monitoring of regional contributions to changes in atmospheric CO_2 .

645

646 **8 Data availability and future update**

647 The CMS-Flux NBE 2020 data are available at: <https://doi.org/10.25966/4v02-c391> (Liu et al.,
648 2020). The regional aggregated fluxes are provided as *csv* files with file size ~10MB, and the
649 gridded data is provided in NetCDF format with file size ~1.4 GB. The full ensemble of posterior
650 fluxes used to estimate posterior flux uncertainties are provided in NetCDF format with file size
651 ~30MB. Table 7 lists the sources of the data used in producing and evaluating the CMS-Flux NBE
652 2020 data product.

653

654 The quality of X_{CO_2} from satellite observations is continually improving. The OCO-2 v10 X_{CO_2}
655 has been released in June 2020 along with the full GOSAT record (June 2009–Jan 2020) processed
656 by the same retrieval algorithm as OCO-2. Continuing to improving the quality of satellite
657 observations and extending the NBE estimates beyond 2018 in the future will help us better
658 understand interactions between terrestrial biosphere carbon cycle and climate and provide support
659 in monitoring the regional contributions to the changes of atmospheric CO_2 . Thus, we plan a future

660 update of the dataset on an annual basis, with a goal to support current scientific research and
661 policy making.

662 **9 Author contributions**

663 JL designed the study and led the writing of the paper in close collaboration with KB and DS. LB
664 helped generate the plots and created all the data files. AAB provided the prior of the terrestrial
665 biosphere carbon fluxes. NP helped interpret the GPP evaluation. DM and DC generated the prior
666 ocean carbon fluxes. TO generated the ODIAC fossil fuel emissions. JJ provided the FLUXSAT
667 GPP product. BD and SW provided and contributed to the interpretation of HIPPO aircraft CO₂
668 observation comparisons. BS, KM, and CS provided ORCAS aircraft CO₂ observations and
669 contributed interpretation of aircraft CO₂ observation comparisons. LVG and JM provided INPE
670 aircraft CO₂ observations and contributed interpretation of aircraft CO₂ observation comparisons.
671 CS and KM provided ATom and the NOAA aircraft CO₂ observations and contributed
672 interpretation of aircraft CO₂ observation comparisons. We furthermore acknowledge funding
673 from the EU for the ERC project “ASICA” (grant number 649087) to Wouter Peters (Groningen
674 University) and EU and NERC (UK) funding to Emanuel Gloor (University of Leeds), which
675 contributed to the INPE Amazon greenhouse sampling program. All authors contributed to the
676 writing, and have reviewed and approved the paper.

677 **10 Competing interest**

678 The authors declare that they have no conflict of interest.

679 **Acknowledgement**

680 Resources supporting this work were provided by the NASA High-End Computing (HEC)
681 Program through the NASA Advanced Supercomputing (NAS) division at Ames Research Center.
682 We acknowledge the funding support from NASA OCO-2/3 Science Team, Carbon Monitoring

683 System (CMS), and Making Earth Science Data Records for Use in Research Environments
684 (MEaSURES) programs. Tomohiro Oda is supported by the NASA Carbon Cycle Science program
685 (grant no. NNX14AM76G). We acknowledge EU and NERC (UK) funding to Emanuel Gloor,
686 University of Leeds which substantially contributed to the INPE Amazon greenhouse sampling
687 program. CarbonTracker Europe results provided by Wageningen University in collaboration with
688 the ObsPack partners (<http://www.carbontracker.eu>). Part of the research was carried out at the Jet
689 Propulsion Laboratory, California Institute of Technology, under a contract with the National
690 Aeronautics and Space Administration (80NM0018D0004)

691

692

693 **Appendix A**

694 As shown in Kalnay (2003):

$$695 \quad RMSE^2 = \frac{1}{n} \sum_{i=1}^n (R_{i,i} + (HP^a H^T)_{i,i}) \quad (A.1)$$

696 where $R_{i,i}$ is the i^{th} aircraft observation error variance, and P^a is the posterior flux error covariance.

697 The H is linearized observation operator, which transfers posterior flux errors to aircraft

698 observation space, and H^T is its adjoint. In the Monte Carlo method, the posterior flux error

699 covariance P^a is approximated by:

$$700 \quad P^a = \frac{1}{n_{ens}} X^a X^{aT} \quad (A.2)$$

701 where X^a is the ensemble perturbations written as:

$$702 \quad X^a = x^a - \bar{x}^a \quad (A.3)$$

703 where x^a is the ensemble posterior fluxes from Monte Carlo, and \bar{x}^a is the mean.

704 Therefore, $HP^a H^T$ can be written as:

$$705 \quad HP^a H^T = \frac{1}{n_{ens}} [h(x^a) - h(\bar{x}^a)][h(x^a) - h(\bar{x}^a)]^T \quad (A.4)$$

706 The sum of diagonal elements in the right-hand side of A.4 is the same as the definition of $RMSE_{MC}$
707 in the main text.

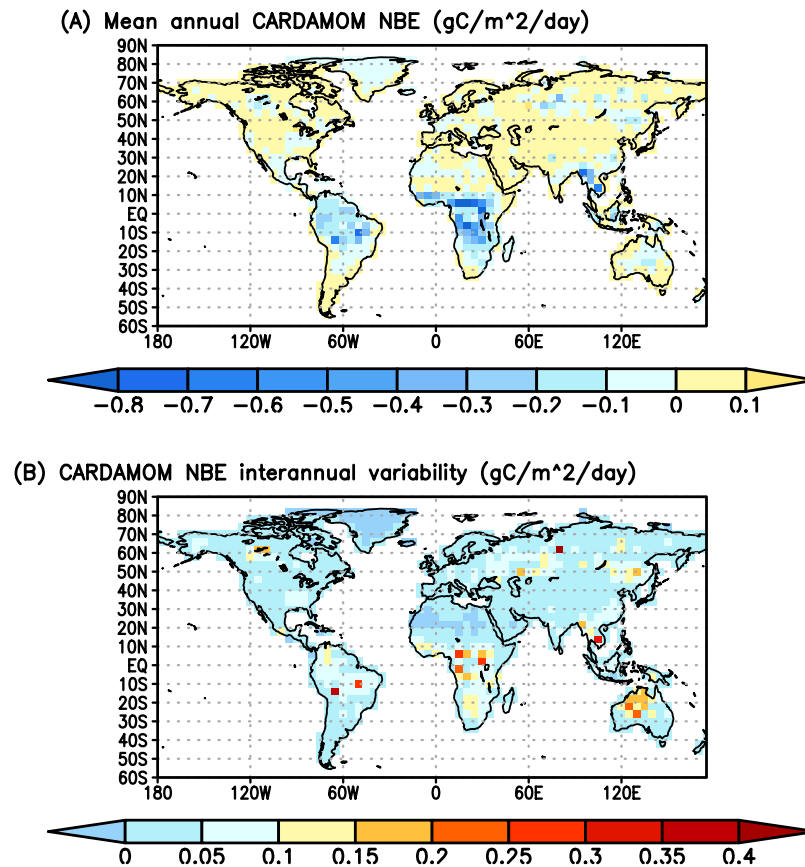
708 Therefore, when the posterior flux uncertainty estimated by Monte Carlo method represents the
709 actual uncertainty in posterior fluxes, equation (A.1) can be written as:

710
$$RMSE^2 = \frac{1}{n} \sum_{i=1}^n R_{i,i} + RMSE_{MC}^2 \quad (A.5).$$

711 It is the same as equation (4) in the main text.

712 Appendix B

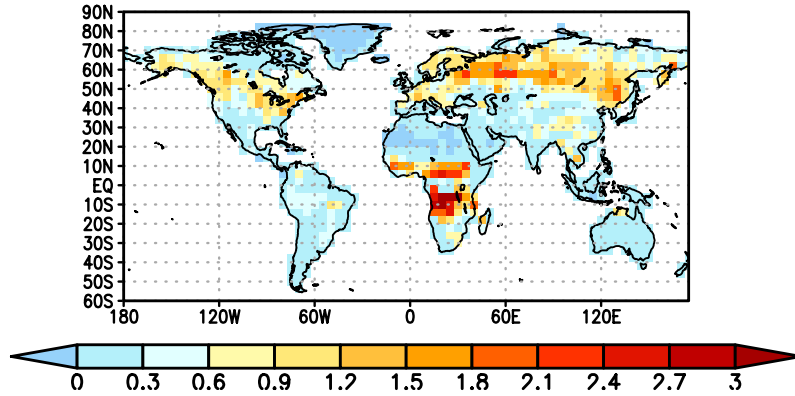
713 In this Appendix, we include figures to support the main text.



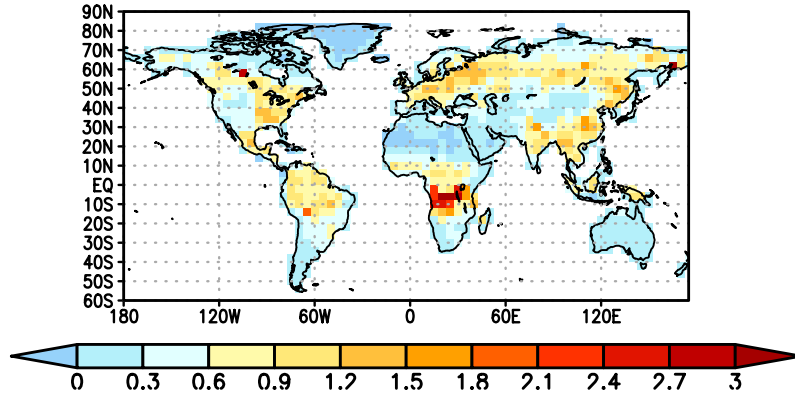
714

715 **Figure B1 Annual mean net biosphere exchanges from CARDAMOM (A) and its interannual**
716 **variability between 2010 and 2017 (B).**

(A) CARDAMOM absolute NBE ($\text{gC}/\text{m}^2/\text{day}$) in July 2010



(B) CARDAMOM NBE uncertainty in July 2010 ($\text{gC}/\text{m}^2/\text{day}$)



717

718

Figure B2 An example of absolute mean NBE (A) and its uncertainty (B) simulated by CARDAMOM. This is for July 2010.

719

720

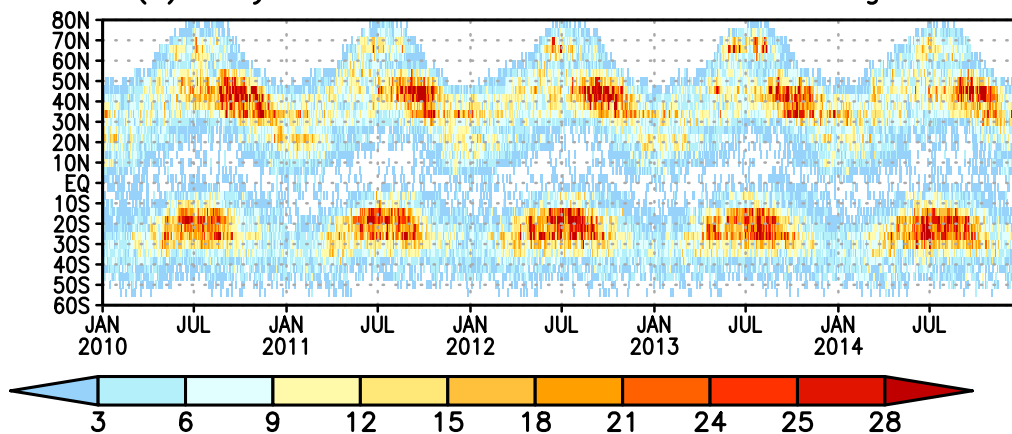
721

722

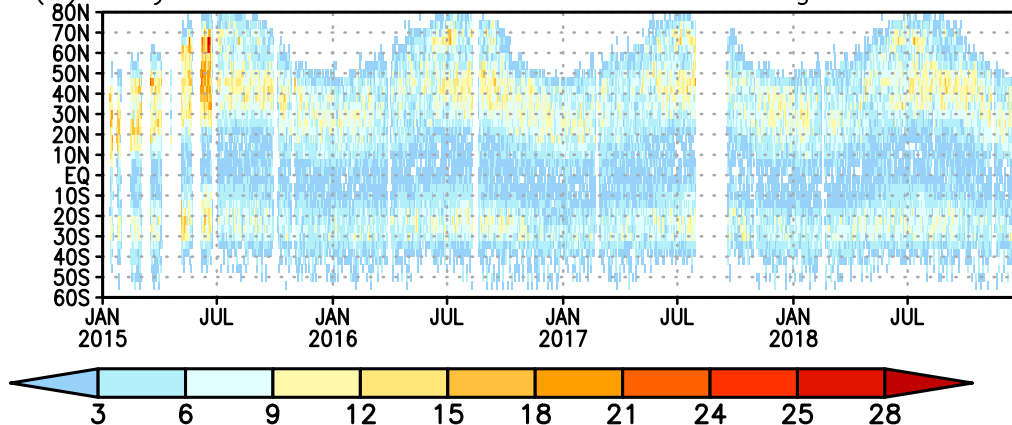
723

724

(A) Daily GOSAT assimilated obs at each 4 degree latitude

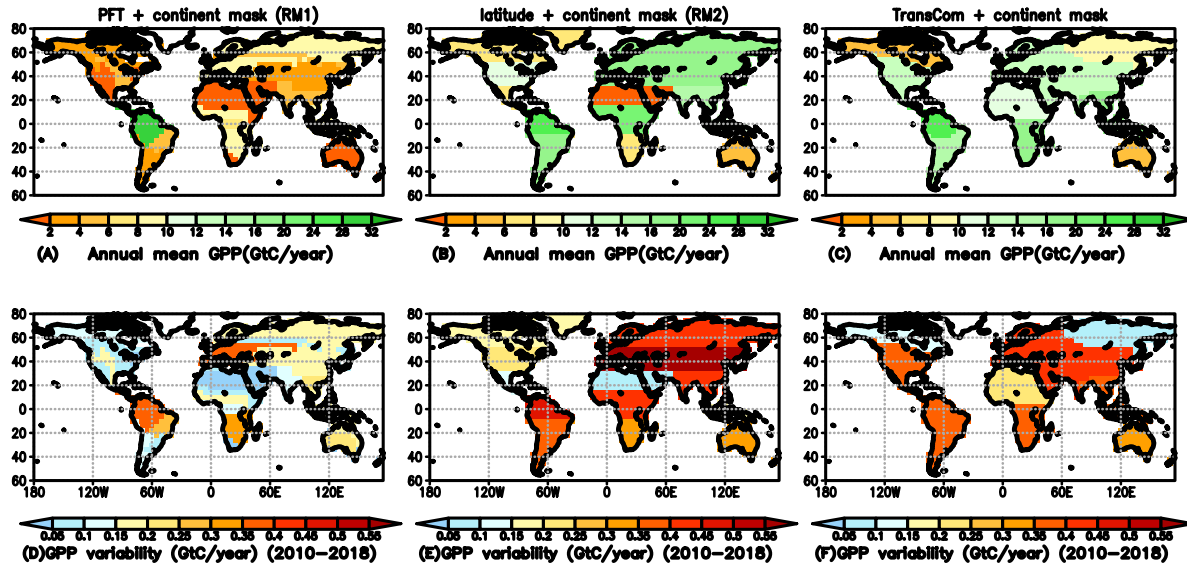


(B) Daily OCO-2 assimilated obs at each 4 degree latitude

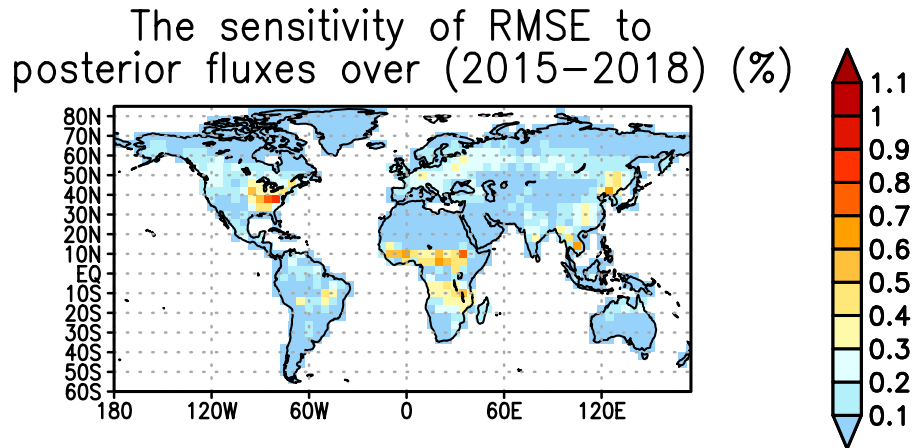


725
726
727
728
729
730
731
732
733

Figure B3 Daily number of ACOS-GOSAT b7.3 (A) and OCO-2 super observations (B) assimilated in the top-down inversions.



734
 735 Figure B4 Regional mean FIUXSAT GPP and its variability between 2010 –2018. (A, B, and C)
 736 Regional mean GPP aggregated with the three regional masks; (D, E, and F) GPP variability
 737 between 2010 –2018. Unit: GtC/year.
 738



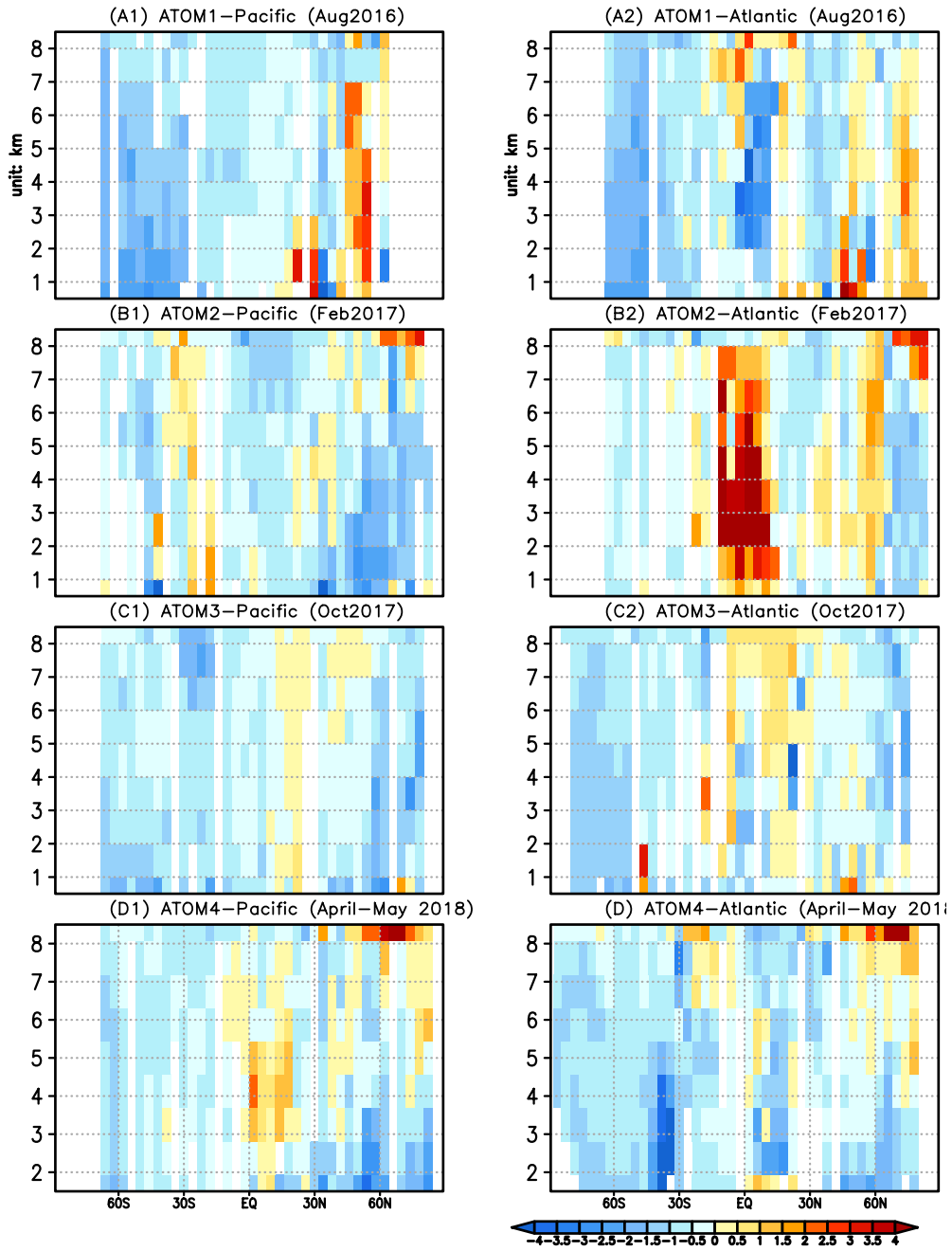
740

741 Figure B5 The relative sensitivity of root mean square errors (RMSE) of posterior CO₂ (Figure 9

742 in the main text) relative to NBE at every grid point. The adjoint model is carried out over Sep

743 2014–Dec 2018.

744

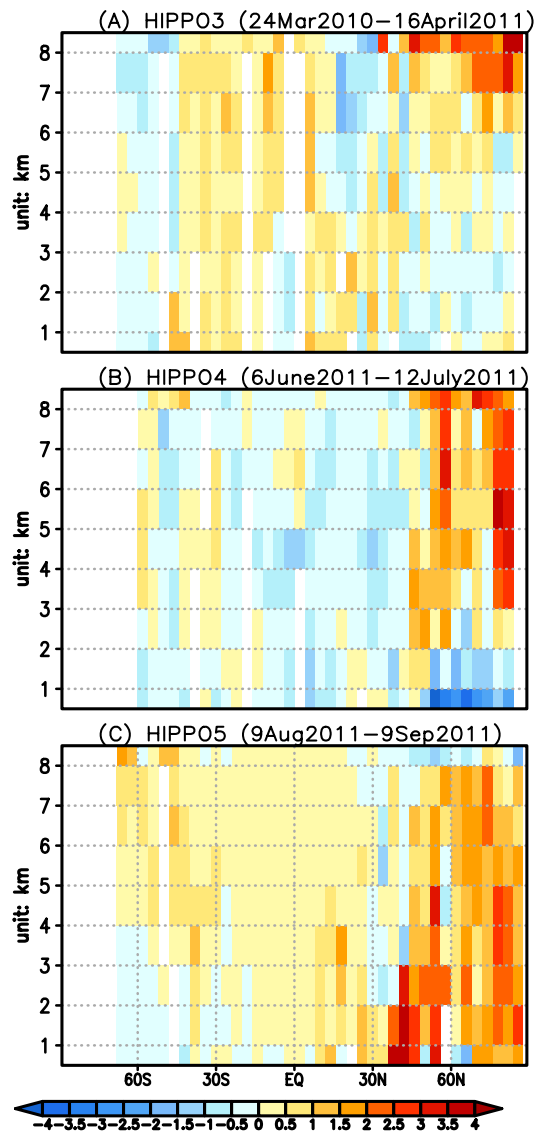


746

747 Figure B6 Differences between posterior CO₂ and ATOM 1-4 aircraft CO₂ observations over the
 748 Pacific (A1-D1) and Atlantic Ocean (A2-D2) as a function of latitude and altitude (unit: km).
 749 Unit: ppm.

750

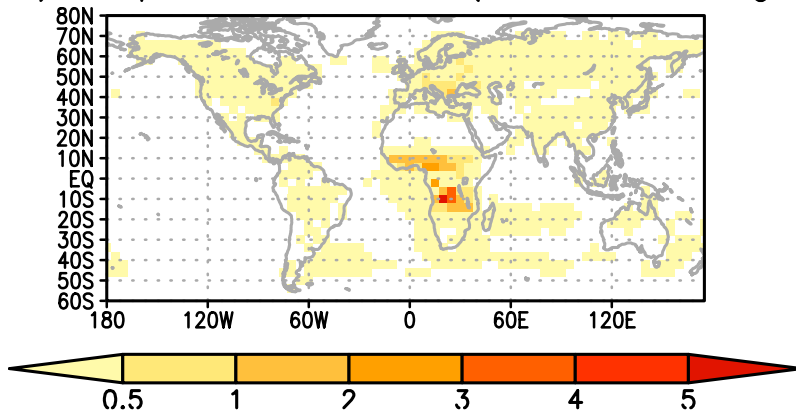
751



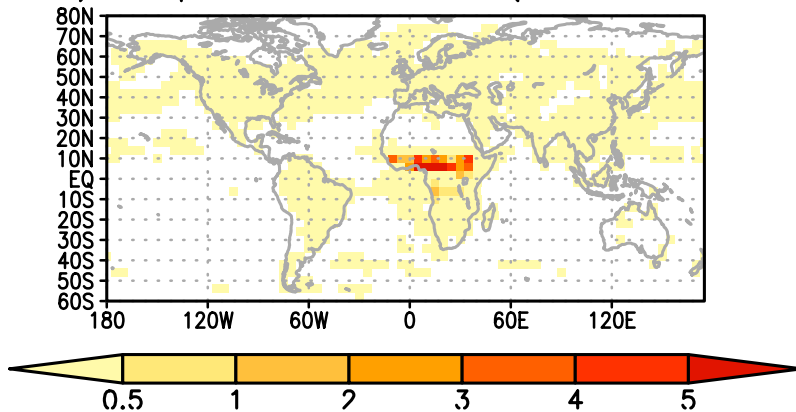
752
 753
 754
 755
 756

Figure B7 Differences between posterior CO₂ and HIPPO 3-5 aircraft CO₂ observations over the Pacific (A-C) as a function of latitude and altitude. Unit: ppm.

A. Relative sensitivity of RMSE between 40W–0, 20S–20N (ATOM–1) to posterior fluxes (June2016–August2016)



B. Relative sensitivity of RMSE between 40W–0, 20S–20N (ATOM–2) to posterior fluxes (Dec2016–Feb2017)

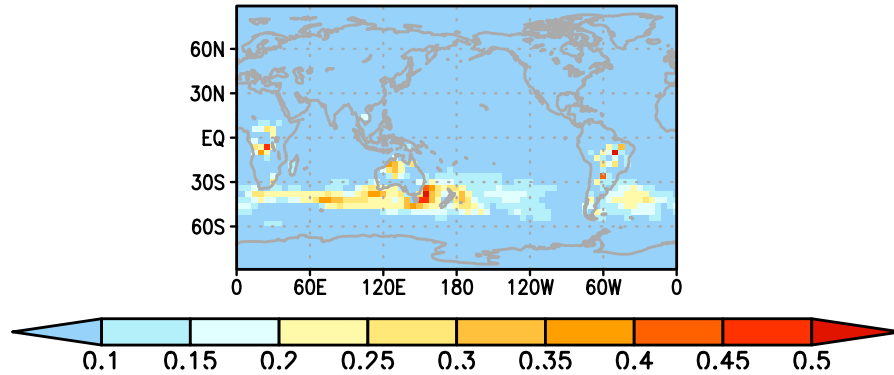


757
 758 Figure B8 The relative sensitivity of RMSE of posterior CO₂ to NBE over land and air-sea net
 759 net carbon exchange over ocean at every grid point. The RMSE is calculated against aircraft CO₂
 760 observations from ATom-1 (A) and ATom-2 (B) between 40°W–0°, 20°S–20°N. The adjoint
 761 model is carried out over June – August 2016 (A) and Dec 2016 – Feb 2017 (B). Unit: %.

762
 763
 764
 765
 766
 767
 768
 769
 770
 771
 772
 773
 774
 775

776
777
778

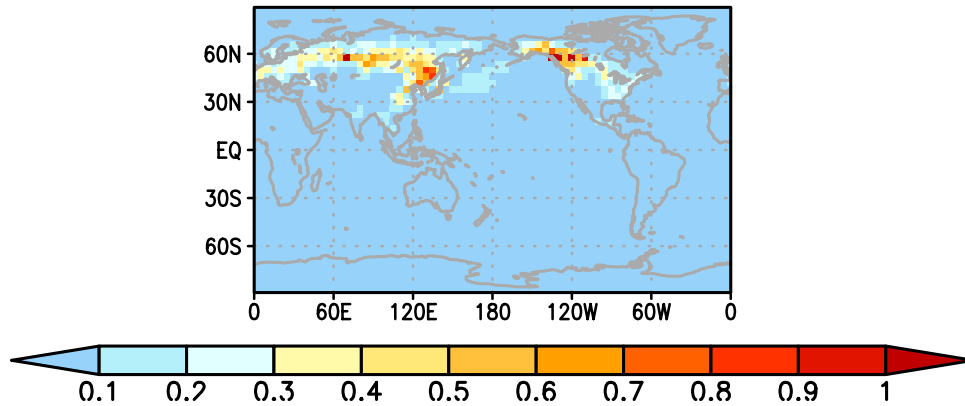
Relative sensitivity of RMSE between 175W–20W, 80S–30S
(ATOM-1) to posterior fluxes (June–August)



779
780
781
782
783
784
785
786
787
788

Figure B9 The relative sensitivity of RMSE of posterior to NBE over land and air-sea net carbon exchange over ocean at every grid point. The RMSE is calculated against aircraft CO₂ observations from ATom-1 between 175°W–20°W, 80°S–30°S. The adjoint model is carried out over June – August 2016. Unit: %.

Relative sensitivity of RMSE between 180W–130W, 50N–90N
(HIPPO-4) to posterior fluxes (Apr–July)



790

791 Figure B10 The relative sensitivity of RMSE of posterior to NBE over land and air-sea net carbon
792 exchange over ocean at every grid point. The RMSE is calculated against aircraft CO₂ observations
793 from HIPPO-4 between 180°W-130°W, 50°N-90°N. The adjoint model is carried out over April
794 – July 2011. Unit: %.

795

796

797

798

799

800

801

802

803

804

805

806

807

808

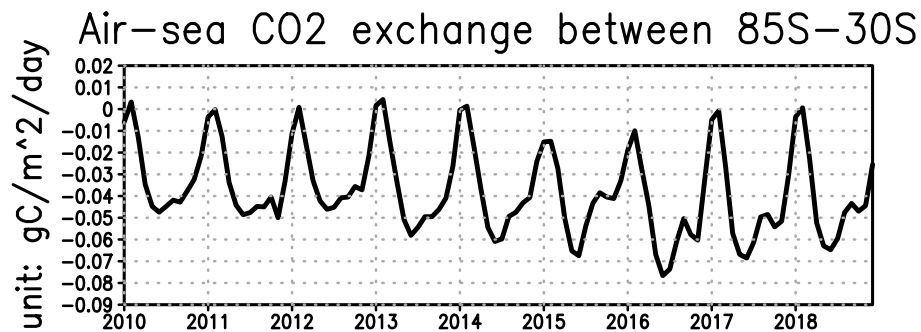
809

810

811

812

813



814
815 Figure B11 Monthly posterior air-sea CO₂ exchanges between 85°S-30°S. (unit: gC/m²/day)
816

817
818 References

819 Arellano Jr, A.F., Kasibhatla, P.S., Giglio, L., Van der Werf, G.R., Randerson, J.T., and Collatz,
820 G.J.: Time-dependent inversion estimates of global biomass-burning CO emissions using
821 Measurement of Pollution in the Troposphere (MOPITT) measurements, *J. Geophys. Res:*
822 *Atmos.*, 111, D09303, <https://doi.org/10.1029/2005JD006613>, 2006.
823
824 Baker, D.F., Doney, S.C., and Schimel, D.S.: Variational data assimilation for atmospheric
825 CO₂, *Tellus B: Chem. Phys. Meteorol.*, 58, 359-365, <https://doi.org/10.1111/j.1600-0889.2006.00218.x>, 2006a.
826
827 Baker, D.F., Law, R.M., Gurney, K.R., Rayner, P., Peylin, P., Denning, A.S., Bousquet, P.,
828 Bruhwiler, L., Chen, Y.H., Ciais, P., and Fung, I.Y.: TransCom 3 inversion intercomparison:
829 Impact of transport model errors on the interannual variability of regional CO₂ fluxes, 1988–
830 2003, *Global Biogeochem. Cy.*, 20, GB1002, <https://doi.org/10.1029/2004GB002439>, 2006b.
831
832 Bastos, A., Friedlingstein, P., Sitch, S., Chen, C., Mialon, A., Wigneron, J.-P., Arora, V.
833 K., Briggs, P. R., Canadell, J. G., and Ciais, P.: Impact of the 2015/2016 El Niño on the terrestrial
834 carbon cycle constrained by bottom-up and top-down approaches. *Philos. Trans. R Soc. Lond. B.*
835 *Biol. Sci.*, 373, 1760, <https://doi.org/10.1098/rstb.2017.0304>, 2018.
836
837 Bloom, A.A., Exbrayat, J.F., van der Velde, I.R., Feng, L., and Williams, M.: The decadal state of
838 the terrestrial carbon cycle: Global retrievals of terrestrial carbon allocation, pools, and residence
839 times. *Proc. Natl Acad. Sci.*, 113, 1285-1290, 2016.
840
841 Bloom, A. A., Bowman, K. W., Liu, J., Konings, A. G., Worden, J. R., Parazoo, N. C., Meyer, V.,
842 Reager, J. T., Worden, H. M., Jiang, Z., Quetin, G. R., Smallman, T. L., Exbrayat, J.-F., Yin, Y.,
843 Saatchi, S. S., Williams, M., and Schimel, D. S.: Lagged effects dominate the inter-annual
844 variability of the 2010–2015 tropical carbon balance, *Biogeosciences Discuss.*,
845 <https://doi.org/10.5194/bg-2019-459>, in review, 2020.
846
847

848 Bowman, K.W., Liu, J., Bloom, A.A., Parazoo, N.C., Lee, M., Jiang, Z., Menemenlis, D., Gierach,
849 M.M., Collatz, G.J., Gurney, K.R., and Wunch, D.: Global and Brazilian carbon response to El
850 Niño Modoki 2011–2010, *Earth Space Sci.*, 4, 637-660, <https://doi.org/10.1002/2016EA000204>,
851 2017.

852

853 Brix, H., Menemenlis, D., Hill, C., Dutkiewicz, S., Jahn, O., Wang, D., Bowman, K., and Zhang,
854 H.: Using Green's Functions to initialize and adjust a global, eddy ocean biogeochemistry
855 general circulation model, *Ocean Model.*, 95, 1-14, <https://doi.org/10.1016/j.ocemod.2015.07.008>,
856 2015.

857

858 Byrd, R.H., Nocedal, J., and Schnabel, R.B.: Representations of quasi-Newton matrices and their
859 use in limited memory methods, *Math. Program.*, 63, 129-156,
860 <https://doi.org/10.1007/BF01582063>, 1994.

861

862 Byrne, B., Liu, J., et al.: Improved constraints on northern extratropical CO₂ fluxes obtained by
863 combining surface-based and space-based atmospheric CO₂ measurements, *JGR-Atmosphere*,
864 (*minor revision*), 2020

865

866 Carroll, D., Menemenlis, D., Adkins, J. F., Bowman, K. W., Brix, H., Dutkiewicz, S., et al.:
867 The ECCO-Darwin Data-assimilative Global Ocean Biogeochemistry Model: Estimates of Seasonal to
868 Multi-decadal Surface Ocean pCO₂ and Air-sea CO₂ Flux. *Journal of Advances in Modeling Earth*
869 *Systems*, 12, e2019MS001888. <https://doi.org/10.1029/2019MS001888>.2020

870

871 Carbontracker Team; (2019) : Compilation of near real time atmospheric carbon dioxide data;
872 obspack_co2_1_NRT_v5.0_2019-08-13; NOAA Earth System Research Laboratory, Global
873 Monitoring Division. <http://doi.org/10.25925/20190813>

874

875 Chevallier, F., Fisher, M., Peylin, P., Serrar, S., Bousquet, P., Bréon, F.M., Chédin, A., and Ciais,
876 P.: Inferring CO₂ sources and sinks from satellite observations: Method and application to TOVS
877 data, *J. Geophys. Res.-Atmos.*, 110, D24309, <https://doi.org/10.1029/2005JD006390>, 2005.

878

879 Chevallier, F., Ciais, P., Conway, T.J., Aalto, T., Anderson, B.E., Bousquet, P., Brunke, E.G.,
880 Ciattaglia, L., Esaki, Y., Fröhlich, M., and Gomez, A.: CO₂ surface fluxes at grid point scale
881 estimated from a global 21 year reanalysis of atmospheric measurements, *J. Geophys. Res.*, 115,
882 D21307, <https://doi.org/10.1029/2010JD013887>, 2010.

883

884 Chevallier, F., Remaud, M., O'Dell, C. W., Baker, D., Peylin, P., and Cozic, A.: Objective
885 evaluation of surface- and satellite-driven carbon dioxide atmospheric inversions, *Atmos. Chem.*
886 *Phys.*, 19, 14233–14251, <https://doi.org/10.5194/acp-19-14233-2019>, 2019.

887

888 Ciais, P., Tan, J., Wang, X., Roedenbeck, C., Chevallier, F., Piao, S.L., Moriarty, R., Broquet, G.,
889 Le Quéré, C., Canadell, J.G., and Peng, S.: Five decades of northern land carbon uptake revealed
890 by the interhemispheric CO₂ gradient, *Nature*, 568, 221-225, [https://doi.org/10.1038/s41586-019-](https://doi.org/10.1038/s41586-019-1078-6)
891 [1078-6](https://doi.org/10.1038/s41586-019-1078-6), 2019.

892

893 Conway, T. J., Tans, P. P., Waterman, L. S., Thoning, K. W., Kitzis, D. R., Masarie, K. A.,
894 and Zhang, N. (1994), Evidence for interannual variability of the carbon cycle from the National

895 Oceanic and Atmospheric Administration/Climate Monitoring and Diagnostics Laboratory Global
896 Air Sampling Network, *J. Geophys. Res.*, 99(D11), 22831– 22855, doi:[10.1029/94JD01951](https://doi.org/10.1029/94JD01951).
897
898
899 Crisp, D., Fisher, B. M., O'Dell, C., Frankenberg, C., Basilio, R., Bösch, H., Brown, L. R., Castano,
900 R., Connor, B., Deutscher, N. M., Eldering, A., Griffith, D., Gunson, M., Kuze, A., Mandrake, L.,
901 McDuffie, J., Messerschmidt, J., Miller, C. E., Morino, I., Natraj, V., Notholt, J., O'Brien, D. M.,
902 Oyafuso, F., Polonsky, I., Robinson, J., Salawitch, R., Sherlock, V., Smyth, M., Suto, H., Taylor,
903 T. E., Thompson, D. R., Wennberg, P. O., Wunch, D., and Yung, Y. L.: The ACOS CO₂ retrieval
904 algorithm – Part II: Global X_{CO2} data characterization, *Atmos. Meas. Tech.*, 5, 687–707,
905 <https://doi.org/10.5194/amt-5-687-2012>, 2012.
906
907 Crisp, D., Pollock, H. R., Rosenberg, R., Chapsky, L., Lee, R. A. M., Oyafuso, F. A., Frankenberg,
908 C., O'Dell, C. W., Bruegge, C. J., Doran, G. B., Eldering, A., Fisher, B. M., Fu, D., Gunson, M.
909 R., Mandrake, L., Osterman, G. B., Schwandner, F. M., Sun, K., Taylor, T. E., Wennberg, P. O.,
910 and Wunch, D.: The on-orbit performance of the Orbiting Carbon Observatory-2 (OCO-2)
911 instrument and its radiometrically calibrated products, *Atmos. Meas. Tech.*, 10, 59–81,
912 <https://doi.org/10.5194/amt-10-59-2017>, 2017.
913
914 Crowell, S., Baker, D., Schuh, A., Basu, S., Jacobson, A. R., Chevallier, F., Liu, J., Deng, F., Feng,
915 L., McKain, K., Chatterjee, A., Miller, J. B., Stephens, B. B., Eldering, A., Crisp, D., Schimel, D.,
916 Nassar, R., O'Dell, C. W., Oda, T., Sweeney, C., Palmer, P. I., and Jones, D. B. A.: The 2015–
917 2016 carbon cycle as seen from OCO-2 and the global in situ network, *Atmos. Chem. Phys.*, 19,
918 9797–9831, <https://doi.org/10.5194/acp-19-9797-2019>, 2019.
919
920 Davis, K.J., M.D. Obland, B. Lin, T. Lauvaux, C. O'Dell, B. Meadows, E.V. Browell, J.P. DiGangi,
921 C. Sweeney, M.J. McGill, J.D. Barrick, A.R. Nehrir, M.M. Yang, J.R. Bennett, B.C. Baier, A.
922 Roiger, S. Pal, T. Gerken, A. Fried, S. Feng, R. Shrestha, M.A. Shook, G. Chen, L.J. Campbell,
923 Z.R. Barkley, and R.M. Pauly. 2018. ACT-America: L3 Merged In Situ Atmospheric Trace Gases
924 and Flask Data, Eastern USA. ORNL DAAC, Oak Ridge, Tennessee, USA.
925 <https://doi.org/10.3334/ORNLDAAC/1593>
926
927 Falk, M., Wharton, S., Schroeder, M., Ustin, S., and U, K.T.P.: Flux partitioning in an old-growth
928 forest: seasonal and interannual dynamics. *Tree Physiol.*, 28, 509-520,
929 <https://doi.org/10.1093/treephys/28.4.509>, 2008.
930
931 Fisher, M. and Courtier, P. (1995) Estimating the covariance matrices of analysis and forecast
932 error in variational data assimilation. Technical Memorandum 220. Reading, UK: ECMWF.
933
934
935 Friedlingstein, P., Meinshausen, M., Arora, V.K., Jones, C.D., Anav, A., Liddicoat, S.K., and
936 Knutti, R.: Uncertainties in CMIP5 climate projections due to carbon cycle feedbacks, *J. Clim.*, 27,
937 511-526, <https://doi.org/10.1175/JCLI-D-12-00579.1>, 2014.
938

939 Friedlingstein, P., Jones, M., O'Sullivan, M., Andrew, R., Hauck, J., Peters, G., Peters, W.,
940 Pongratz, J., Sitch, S., Le Quéré, C., and DBakker, O.: Global carbon budget 2019, *Earth Syst. Sci.*
941 *Data*, 11, 1783-1838, <https://doi.org/10.3929/ethz-b-000385668>, 2019.

942

943 Gatti, L.V., Gloor, M., Miller, J.B., Doughty, C.E., Malhi, Y., Domingues, L.G., Basso, L.S.,
944 Martinewski, A., Correia, C.S.C., Borges, V.F., and Freitas, S., 2014, Drought sensitivity of
945 Amazonian carbon balance revealed by atmospheric measurements, *Nature*, 506, 76-80,
946 <https://doi.org/10.1038/nature12957>, 2014.

947

948 Gaubert, B., Stephens, B. B., Basu, S., Chevallier, F., Deng, F., Kort, E. A., Patra, P. K., Peters,
949 W., Rödenbeck, C., Saeki, T., Schimel, D., Van der Laan-Luijkx, I., Wofsy, S., and Yin, Y.: Global
950 atmospheric CO₂ inverse models converging on neutral tropical land exchange, but disagreeing on
951 fossil fuel and atmospheric growth rate, *Biogeosciences*, 16, 117–134, [https://doi.org/10.5194/bg-](https://doi.org/10.5194/bg-16-117-2019)
952 16-117-2019, 2019.

953

954

955 Gurney, K.R., Law, R.M., Denning, A.S., Rayner, P.J., Pak, B.C., Baker, D., Bousquet, P.,
956 Bruhwiler, L., Chen, Y.H., Ciais, P., and Fung, I.Y.: Transcom 3 inversion intercomparison: Model
957 mean results for the estimation of seasonal carbon sources and sinks, *Global Biogeochem.*
958 *Cycles*, 18, GB1010, <https://doi.org/10.1029/2003GB002111>, 2004.

959

960 Henze, D. K., Hakami, A., and Seinfeld, J. H.: Development of the adjoint of GEOS-Chem, *Atmos.*
961 *Chem. Phys.*, 7, 2413–2433, <https://doi.org/10.5194/acp-7-2413-2007>, 2007.

962

963 IPCC (2018). *Global warming of 1.5°C. An IPCC Special Report on the impacts of global*
964 *warming of 1.5°C above pre-industrial levels and related global greenhouse gas emission*
965 *pathways, in the context of strengthening the global response to the threat of climate change,*
966 *sustainable development, and efforts to eradicate poverty* [V. Masson-Delmotte, P. Zhai, H. O.
967 Pörtner, D. Roberts, J. Skea, P. R. Shukla, A. Pirani, W. Moufouma-Okia, C. Péan, R. Pidcock,
968 S. Connors, J. B. R. Matthews, Y. Chen, X. Zhou, M. I. Gomis, E. Lonnoy, T. Maycock, M.
969 Tignor, T. Waterfield (eds.)]. In Press.

970

971 Jiang, Z., Worden, J. R., Worden, H., Deeter, M., Jones, D. B. A., Arellano, A. F., and Henze, D.
972 K.: A 15-year record of CO emissions constrained by MOPITT CO observations, *Atmos. Chem.*
973 *Phys.*, 17, 4565–4583, <https://doi.org/10.5194/acp-17-4565-2017>, 2017.

974

975 Joiner, J., Guanter, L., Lindstrot, R., Voigt, M., Vasilkov, A. P., Middleton, E. M., Huemmrich, K.
976 F., Yoshida, Y., and Frankenberg, C.: Global monitoring of terrestrial chlorophyll fluorescence
977 from moderate-spectral-resolution near-infrared satellite measurements: methodology,
978 simulations, and application to GOME-2, *Atmos. Meas. Tech.*, 6, 2803–2823,
979 <https://doi.org/10.5194/amt-6-2803-2013>, 2013.

980

981 Joiner, J., Yoshida, Y., Zhang, Y., Duveiller, G., Jung, M., Lyapustin, A., Wang, Y., & Tucker,
982 C.: Estimation of terrestrial global gross primary production (GPP) with satellite data-driven
983 models and eddy covariance flux data. *Remote*
984 *Sensing*, 10(9), 1346. <https://doi.org/10.3390/rs10091346>. 2018.

985
986 Jones, D. B. A., Bowman, K. W., Logan, J. A., Heald, C. L., Liu, J., Luo, M., Worden, J., and
987 Drummond, J.: The zonal structure of tropical O₃ and CO as observed by the Tropospheric
988 Emission Spectrometer in November 2004 – Part 1: Inverse modeling of CO emissions, *Atmos.*
989 *Chem. Phys.*, 9, 3547–3562, <https://doi.org/10.5194/acp-9-3547-2009>, 2009.
990
991 Jung, Martin, et al.: "Compensatory water effects link yearly global land CO₂ sink changes to
992 temperature." *Nature* 541.7638 (2017): 516-520.
993
994 Kiel, M., O'Dell, C. W., Fisher, B., Eldering, A., Nassar, R., MacDonald, C. G., and Wennberg, P.
995 O.: How bias correction goes wrong: measurement of X_{CO₂} affected by erroneous surface pressure
996 estimates, *Atmos. Meas. Tech.*, 12, 2241–2259, <https://doi.org/10.5194/amt-12-2241-2019>, 2019.
997
998 Konings, A. G., Bloom, A. A., Liu, J., Parazoo, N. C., Schimel, D. S., and Bowman, K. W.: Global
999 satellite-driven estimates of heterotrophic respiration, *Biogeosciences*, 16, 2269–2284,
1000 <https://doi.org/10.5194/bg-16-2269-2019>, 2019.
1001
1002 Kulawik, S. S., Crowell, S., Baker, D., Liu, J., McKain, K., Sweeney, C., Biraud, S. C., Wofsy, S.,
1003 O'Dell, C. W., Wennberg, P. O., Wunch, D., Roehl, C. M., Deutscher, N. M., Kiel, M., Griffith,
1004 D. W. T., Velazco, V. A., Notholt, J., Warneke, T., Petri, C., De Mazière, M., Sha, M. K.,
1005 Sussmann, R., Rettinger, M., Pollard, D. F., Morino, I., Uchino, O., Hase, F., Feist, D. G., Roche,
1006 S., Strong, K., Kivi, R., Iraci, L., Shiomi, K., Dubey, M. K., Sepulveda, E., Rodriguez, O. E. G.,
1007 Té, Y., Jeseck, P., Heikkinen, P., Dlugokencky, E. J., Gunson, M. R., Eldering, A., Crisp, D.,
1008 Fisher, B., and Osterman, G. B.: Characterization of OCO-2 and ACOS-GOSAT biases and errors
1009 for CO₂ flux estimates, *Atmos. Meas. Tech. Discuss.*, <https://doi.org/10.5194/amt-2019-257>, in
1010 review, 2019.
1011
1012 Kuze, A., Suto, H., Shiomi, K., Kawakami, S., Tanaka, M., Ueda, Y., Deguchi, A., Yoshida, J.,
1013 Yamamoto, Y., Kataoka, F., Taylor, T. E., and Buijs, H. L.: Update on GOSAT TANSO-FTS
1014 performance, operations, and data products after more than 6 years in space, *Atmos. Meas. Tech.*,
1015 9, 2445–2461, <https://doi.org/10.5194/amt-9-2445-2016>, 2016.
1016
1017 Le Quéré, C., Andrew, R. M., Friedlingstein, P., Sitch, S., Pongratz, J., Manning, A. C.,
1018 Korsbakken, J. I., Peters, G. P., Canadell, J. G., Jackson, R. B., Boden, T. A., Tans, P. P., Andrews,
1019 O. D., Arora, V. K., Bakker, D. C. E., Barbero, L., Becker, M., Betts, R. A., Bopp, L., Chevallier,
1020 F., Chini, L. P., Ciais, P., Cosca, C. E., Cross, J., Currie, K., Gasser, T., Harris, I., Hauck, J., Haverd,
1021 V., Houghton, R. A., Hunt, C. W., Hurtt, G., Ilyina, T., Jain, A. K., Kato, E., Kautz, M., Keeling,
1022 R. F., Klein Goldewijk, K., Körtzinger, A., Landschützer, P., Lefèvre, N., Lenton, A., Lienert, S.,
1023 Lima, I., Lombardozzi, D., Metzl, N., Millero, F., Monteiro, P. M. S., Munro, D. R., Nabel, J. E.
1024 M. S., Nakaoka, S., Nojiri, Y., Padin, X. A., Peregon, A., Pfeil, B., Pierrot, D., Poulter, B., Rehder,
1025 G., Reimer, J., Rödenbeck, C., Schwinger, J., Séférian, R., Skjelvan, I., Stocker, B. D., Tian, H.,
1026 Tilbrook, B., Tubiello, F. N., van der Laan-Luijkx, I. T., van der Werf, G. R., van Heuven, S.,
1027 Viovy, N., Vuichard, N., Walker, A. P., Watson, A. J., Wiltshire, A. J., Zaehle, S., and Zhu, D.:
1028 Global Carbon Budget 2017, *Earth Syst. Sci. Data*, 10, 405–448, [https://doi.org/10.5194/essd-10-](https://doi.org/10.5194/essd-10-405-2018)
1029 405-2018, 2018.
1030

1031 Liu, J., Baskarran, L., Bowman, K., Schimel, D., Bloom, A. A., Parazoo, N., Oda, T., Carrol, D.,
1032 Menemenlis, D., Joiner, J., Commane, R., Daube, B., Gatti, L. V., McKain, K., Miller, J.,
1033 Stephens, B. B., Sweeney, C., & Wofsy, S. (2020). *CMS-Flux NBE 2020* [Data set]. NASA.
1034 <https://doi.org/10.25966/4V02-C391>
1035

1036 Liu, J. and Bowman, K.: A method for independent validation of surface fluxes from atmospheric
1037 inversion: Application to CO₂, *Geophys. Res. Lett.*, 43, 3502-3508,
1038 <https://doi.org/10.1002/2016GL067828>, 2016.
1039

1040 Liu, J., Bowman, K. W., and Henze, D. K.: Source-receptor relationships of column-average
1041 CO₂ and implications for the impact of observations on flux inversions. *J. Geophys. Res.*
1042 *Atmos.*, 120, 5214–5236. doi: [10.1002/2014JD022914](https://doi.org/10.1002/2014JD022914), 2015
1043

1044 Liu, J., Bowman, K.W., Lee, M., Henze, D.K., Bousserez, N., Brix, H., James Collatz, G.,
1045 Menemenlis, D., Ott, L., Pawson, S., and Jones, D.: Carbon monitoring system flux estimation and
1046 attribution: impact of ACOS-GOSAT XCO₂ sampling on the inference of terrestrial biospheric
1047 sources and sinks. *Tellus B Chem. Phys. Meteorol. B.*, 66, 22486,
1048 <http://dx.doi.org/10.3402/tellusb.v66.22486>, 2014.
1049

1050 Liu, J., Bowman, K.W., Schimel, D.S., Parazoo, N.C., Jiang, Z., Lee, M., Bloom, A.A., Wunch,
1051 D., Frankenberg, C., Sun, Y., and O'Dell, C.W.: Contrasting carbon cycle responses of the tropical
1052 continents to the 2015–2016 El Niño. *Science*, 358, eaam5690,
1053 <https://doi.org/10.1126/science.aam5690>, 2017.
1054

1055 Liu, J., Bowman, K., Parazoo, N.C., Bloom, A.A., Wunch, D., Jiang, Z., Gurney, K.R., and
1056 Schimel, D.: Detecting drought impact on terrestrial biosphere carbon fluxes over contiguous US
1057 with satellite observations. *Environ. Res. Lett.*, 13, 095003, [https://doi.org/10.1088/1748-](https://doi.org/10.1088/1748-9326/aad5ef)
1058 [9326/aad5ef](https://doi.org/10.1088/1748-9326/aad5ef), 2018.
1059

1060 Liu, Z.-Q. and Rabier, F. (2003), The potential of high-density observations for numerical
1061 weather prediction: A study with simulated observations. *Q.J.R. Meteorol. Soc.*, 129: 3013-3035.
1062 doi:[10.1256/qj.02.170](https://doi.org/10.1256/qj.02.170)
1063
1064

1065 Lorenc, A. C., 1981: A Global Three-Dimensional Multivariate Statistical Interpolation
1066 Scheme. *Mon. Wea. Rev.*, **109**, 701–721
1067
1068

1069 Lovenduski, N.S. and Bonan, G.B.: Reducing uncertainty in projections of terrestrial carbon
1070 uptake, *Environ. Res. Lett.*, 12, 044020, <https://doi.org/10.1088/1748-9326/aa66b8>, 2017.
1071

1072 Meirink, J.F., Bergamaschi, P. and Krol, M.C. (2008) Four-dimensional variational data
1073 assimilation for inverse modelling of atmospheric methane emissions: method and comparison
1074 with synthesis inversion, *Atmos. Chem. Phys.*, **8**, 6341–6353, [https://doi.org/10.5194/acp-8-](https://doi.org/10.5194/acp-8-6341-2008)
1075 [6341-2008](https://doi.org/10.5194/acp-8-6341-2008).
1076

1077 Nassar, R., Jones, D.B., Suntharalingam, P., Chen, J.M., Andres, R.J., Wecht, K.J., Yantosca, R.M.,
1078 Kulawik, S.S., Bowman, K.W., Worden, J.R., and Machida, T.: Modeling global atmospheric CO₂
1079 with improved emission inventories and CO₂ production from the oxidation of other carbon
1080 species. *Geosci. Model Dev.*, 3, 689–716, <https://doi.org/10.5194/gmd-3-689-2010>, 2010.

1081
1082 Niwa, Y, Fujii, Y. A conjugate BFGS method for accurate estimation of a posterior error
1083 covariance matrix in a linear inverse problem. *Q J R Meteorol*
1084 *Soc.* 2020; 1– 26. <https://doi.org/10.1002/qj.3838>

1085
1086 Oda, T., Maksyutov, S., and Andres, R. J.: The Open-source Data Inventory for Anthropogenic
1087 CO₂, version 2016 (ODIAC2016): a global monthly fossil fuel CO₂ gridded emissions data product
1088 for tracer transport simulations and surface flux inversions, *Earth Syst. Sci. Data*, 10, 87–107,
1089 <https://doi.org/10.5194/essd-10-87-2018>, 2018.

1090
1091 O'Dell, C. W., Connor, B., Bösch, H., O'Brien, D., Frankenberg, C., Castano, R., Christi, M.,
1092 Eldering, D., Fisher, B., Gunson, M., McDuffie, J., Miller, C. E., Natraj, V., Oyafuso, F., Polonsky,
1093 I., Smyth, M., Taylor, T., Toon, G. C., Wennberg, P. O., and Wunch, D.: The ACOS CO₂ retrieval
1094 algorithm – Part 1: Description and validation against synthetic observations, *Atmos. Meas. Tech.*,
1095 5, 99–121, <https://doi.org/10.5194/amt-5-99-2012>, 2012.

1096
1097 O'Dell, C., Eldering, A., Wennberg, P.O., Crisp, D., Gunson, M., Fisher, B., Frankenberg, C., Kiel,
1098 M., Lindqvist, H., Mandrake, L., and Merrelli, A.: Improved retrievals of carbon dioxide from
1099 Orbiting Carbon Observatory-2 with the version 8 ACOS algorithm, *Atmos. Meas. Tech.*, 11,
1100 6539–6576, <https://doi.org/10.5194/amt-11-6539-2018>, 2018.

1101
1102 Olsen, S.C. and Randerson, J.T.: Differences between surface and column atmospheric CO₂ and
1103 implications for carbon cycle research, *J. Geophys. Res: Atmos.*, 109, D02301,
1104 <https://doi.org/10.1029/2003JD003968>, 2004.

1105
1106 Osterman, G., O'Dell, C., Eldering, A.: Data Product User's Guide, Operational Level 2 Data
1107 Versions 10 and Lite File Version 10 and VEarly.
1108 https://docs.server.gesdisc.eosdis.nasa.gov/public/project/OCO/OCO2_OCO3_B10_DUG.pdf,
1109 2020.

1110
1111 Parazoo, N.C., Bowman, K., Fisher, J.B., Frankenberg, C., Jones, D.B.A., Cescatti, A., Pérez-
1112 Priego, Ó., Wohlfahrt, G. and Montagnani, L.: Terrestrial gross primary production inferred from
1113 satellite fluorescence and vegetation models. *Glob Change Biol*, 20: 3103-3121.
1114 doi:[10.1111/gcb.12652](https://doi.org/10.1111/gcb.12652). 2014.

1115
1116 Peylin, P., Law, R. M., Gurney, K. R., Chevallier, F., Jacobson, A. R., Maki, T., Niwa, Y., Patra,
1117 P. K., Peters, W., Rayner, P. J., Rödenbeck, C., van der Laan-Luijkx, I. T., and Zhang, X.: Global
1118 atmospheric carbon budget: results from an ensemble of atmospheric CO₂ inversions,
1119 *Biogeosciences*, 10, 6699–6720, <https://doi.org/10.5194/bg-10-6699-2013>, 2013.

1120
1121

1122 Peters, W., et al. (2007), An atmospheric perspective on North American carbon dioxide exchange:
1123 CarbonTracker, *Proc. Natl. Acad. Sci. U. S. A.*, **104**(48), 18,925– 18,930,
1124 doi:[10.1073/pnas.0708986104](https://doi.org/10.1073/pnas.0708986104).
1125
1126 Peters, W., Krol, M. C., Van Der Werf, G.R., et al, 2010, Seven years of recent European net
1127 terrestrial carbon dioxide exchange constrained by atmospheric observations. *Global Change*
1128 *Biology*, 16: 1317-1337. doi:[10.1111/j.1365-2486.2009.02078.x](https://doi.org/10.1111/j.1365-2486.2009.02078.x)
1129
1130
1131 Poulter, B., Frank, D., Ciais, P., Myneni, R.B., Andela, N., Bi, J., Broquet, G., Canadell, J.G.,
1132 Chevallier, F., Liu, Y.Y., and Running, S.W.: Contribution of semi-arid ecosystems to interannual
1133 variability of the global carbon cycle, *Nature*, 509, 600-603, <https://doi.org/10.1038/nature13376>,
1134 2014.
1135
1136 Quetin, G., Bloom, A. A., Bowman, K. W., & Konings, A.: Carbon flux variability from a
1137 relatively simple ecosystem model with assimilated data is consistent with terrestrial biosphere
1138 model estimates. *Journal of Advances in Modeling Earth Systems*, 12,
1139 e2019MS001889. <https://doi.org/10.1029/2019MS001889>, 2020
1140
1141 Randerson, J.T., Van Der Werf, G.R., Giglio, L., Collatz, G.J., and Kasibhatla, P.S.: Global Fire
1142 Emissions Database, Version 4.1 (GFEDv4), ORNL DAAC, Oak Ridge, Tennessee,
1143 USA, <https://doi.org/10.3334/ORNLDAAC/1293>, 2018.
1144
1145 Rienecker, M.M., Suarez, M.J., Gelaro, R., Todling, R., Bacmeister, J., Liu, E., Bosilovich, M.G.,
1146 Schubert, S.D., Takacs, L., Kim, G.K., and Bloom, S.: MERRA: NASA's modern-era
1147 retrospective analysis for research and applications, *J. Clim.*, 24, 3624-3648,
1148 <https://doi.org/10.1175/JCLI-D-11-00015.1>, 2011.
1149
1150 Rödenbeck, C., Houweling, S., Gloor, M., and Heimann, M.: CO₂ flux history 1982–2001 inferred
1151 from atmospheric data using a global inversion of atmospheric transport, *Atmos. Chem. Phys.*, 3,
1152 1919–1964, <https://doi.org/10.5194/acp-3-1919-2003>, 2003.
1153
1154
1155 Running, S.W., Baldocchi, D.D., Turner, D.P., Gower, S.T., Bakwin, P.S., and Hibbard, K.A.: A
1156 global terrestrial monitoring network integrating tower fluxes, flask sampling, ecosystem
1157 modeling and EOS satellite data, *Remote Sens. Environ.*, 70, 108-127,
1158 [https://doi.org/10.1016/S0034-4257\(99\)00061-9](https://doi.org/10.1016/S0034-4257(99)00061-9), 1999.
1159
1160 Schuh, A.E., Jacobson, A.R., Basu, S., Weir, B., Baker, D., Bowman, K., Chevallier, F., Crowell,
1161 S., Davis, K.J., Deng, F., and Denning, S.: Quantifying the impact of atmospheric transport
1162 uncertainty on CO₂ surface flux estimates, *Global Biogeochem. Cy.*, 33, 484-500,
1163 <https://doi.org/10.1029/2018GB006086>, 2019.
1164
1165 Sellers, P.J., Schimel, D.S., Moore, B., Liu, J., and Eldering, A.: Observing carbon cycle–climate
1166 feedbacks from space, *PNAS*, 115, 7860-7868, <https://doi.org/10.1073/pnas.1716613115>, 2018.
1167

1168 Stephens, B.B., Gurney, K. R., Tans, P. P., *et al.*: Weak northern and strong tropical land carbon
1169 uptake from vertical profiles of atmospheric CO₂. *Science* **316**: 1732– 35,
1170 doi:10.1126/science.1137004. 2007
1171

1172 Stephens, B., et al. 2017. ORCAS Airborne Oxygen Instrument. Version 1.0. UCAR/NCAR -
1173 Earth Observing Laboratory. <https://doi.org/10.5065/D6N29VC6>.

1174 Sweeney, C., Karion, A., Wolter, S., et al.: Seasonal climatology of CO₂ across North America
1175 from aircraft measurements in the NOAA/ESRL Global Greenhouse Gas Reference Network. *J.*
1176 *Geophys. Res. Atmos.*, 120, 5155– 5190. doi: [10.1002/2014JD022591](https://doi.org/10.1002/2014JD022591). 2015

1177

1178 Suntharalingam, P., Jacob, D.J., Palmer, P.I., Logan, J.A., Yantosca, R.M., Xiao, Y., Evans, M.J.,
1179 Streets, D.G., Vay, S.L., and Sachse, G.W.: Improved quantification of Chinese carbon fluxes
1180 using CO₂/CO correlations in Asian outflow, *J. Geophys. Res.: Atmos.*, 109, D18S18,
1181 <https://doi.org/10.1029/2003JD004362>, 2004.
1182

1183 Tramontana, G., Jung, M., Schwalm, C. R., Ichii, K., Camps-Valls, G., Ráduly, B., Reichstein, M.,
1184 Arain, M. A., Cescatti, A., Kiely, G., Merbold, L., Serrano-Ortiz, P., Sickert, S., Wolf, S., and
1185 Papale, D.: Predicting carbon dioxide and energy fluxes across global FLUXNET sites with
1186 regression algorithms, *Biogeosciences*, 13, 4291–4313, <https://doi.org/10.5194/bg-13-4291-2016>,
1187 2016.
1188

1189 van der Laan-Luijkx et al, 2017, "The CarbonTracker Data Assimilation Shell (CTDAS) v1.0:
1190 implementation and global carbon balance 2001-2015", [Geosci. Model Dev.](https://doi.org/10.5194/gmd-10-2785-2017), **10**, 2785-2800,
1191

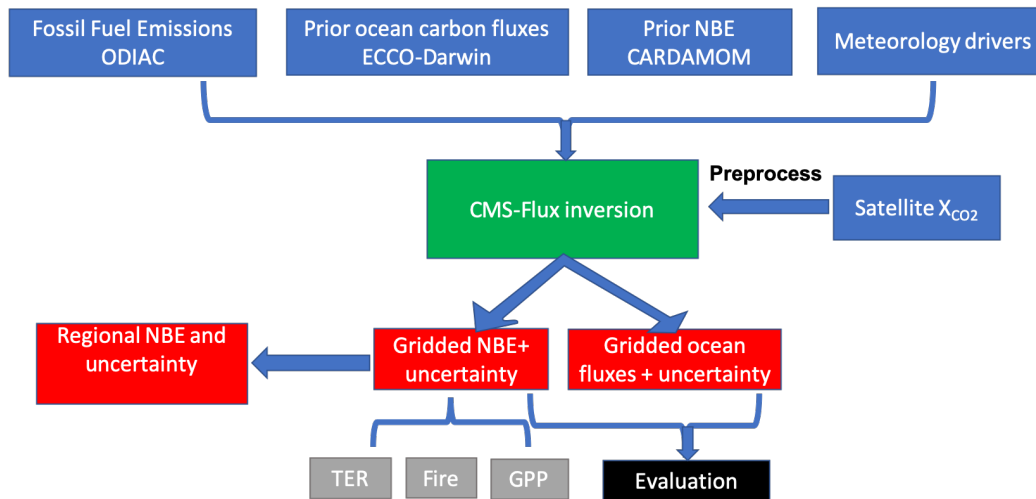
1192 van der Werf, G. R., Randerson, J. T., Giglio, L., Gobron, N., and Dolman, A. J.: Climate
1193 controls on the variability of fires in the tropics and subtropics, *Global Biogeochem. Cycles*, **22**,
1194 GB3028, doi:[10.1029/2007GB003122](https://doi.org/10.1029/2007GB003122). 2008
1195
1196
1197

1198 Wofsy, S. C.: HIAPER Pole-to-Pole Observations (HIPPO): Fine-grained, global-scale
1199 measurements of climatically important atmospheric gases and aerosols, *Philos. Trans. R. Soc. A-*
1200 *Math. Phys. Eng. Sci.*, 369, 2073– 2086, <https://doi.org/10.1098/rsta.2010.0313>, 2011.
1201

1202 Wofsy, S.C., Afshar, S., Allen, H.M., Apel, E., Asher, E.C., Barletta, B., Bent, J., Bian, H., Biggs,
1203 B.C., Blake, D.R., and Blake, N.: ATom: Merged Atmospheric Chemistry, Trace Gases, and
1204 Aerosols, ORNL DAAC, Oak Ridge, Tennessee,
1205 USA, <https://doi.org/10.3334/ORNLLDAAC/1581>, 2018.
1206

1207 Wunch, D., Toon, G.C., Blavier, J.F.L., Washenfelder, R.A., Notholt, J., Connor, B.J., Griffith,
1208 D.W., Sherlock, V., and Wennberg, P.O.: The total carbon column observing network, *Philos.*
1209 *Trans. R. Soc. A*, 369, 2087-2112, <https://doi.org/10.1098/rsta.2010.0240>, 2011.
1210

1211 Yin, Y., Bowman, K., Bloom, A.A., and Worden, J.: Detection of fossil fuel emission trends in the
1212 presence of natural carbon cycle variability, *Environ. Res. Lett.*, 14, 084050,
1213 <https://doi.org/10.1088/1748-9326/ab2dd7>, 2019.
1214
1215 Zhu, C., Byrd, R.H., Lu, P., and Nocedal, J.: Algorithm 778: L-BFGS-B: Fortran subroutines for
1216 large-scale bound-constrained optimization, *ACM Trans. Math. Softw.*, 23, 550-560,
1217 <https://doi.org/10.1145/279232.279236>, 1997.
1218
1219
1220



1221

1222 **Figure: 1 Data flow diagram with the main processing steps to generate regional net**
 1223 **biosphere change (NBE). TER: total ecosystem respiration; GPP: gross primary production.**
 1224 **The green box is the inversion system. The blue boxes are the inputs for the inversion system.**
 1225 **The red boxes are the data outputs from the system. The black box is the evaluation step,**
 1226 **and the grey boxes are the future additions to the product.**

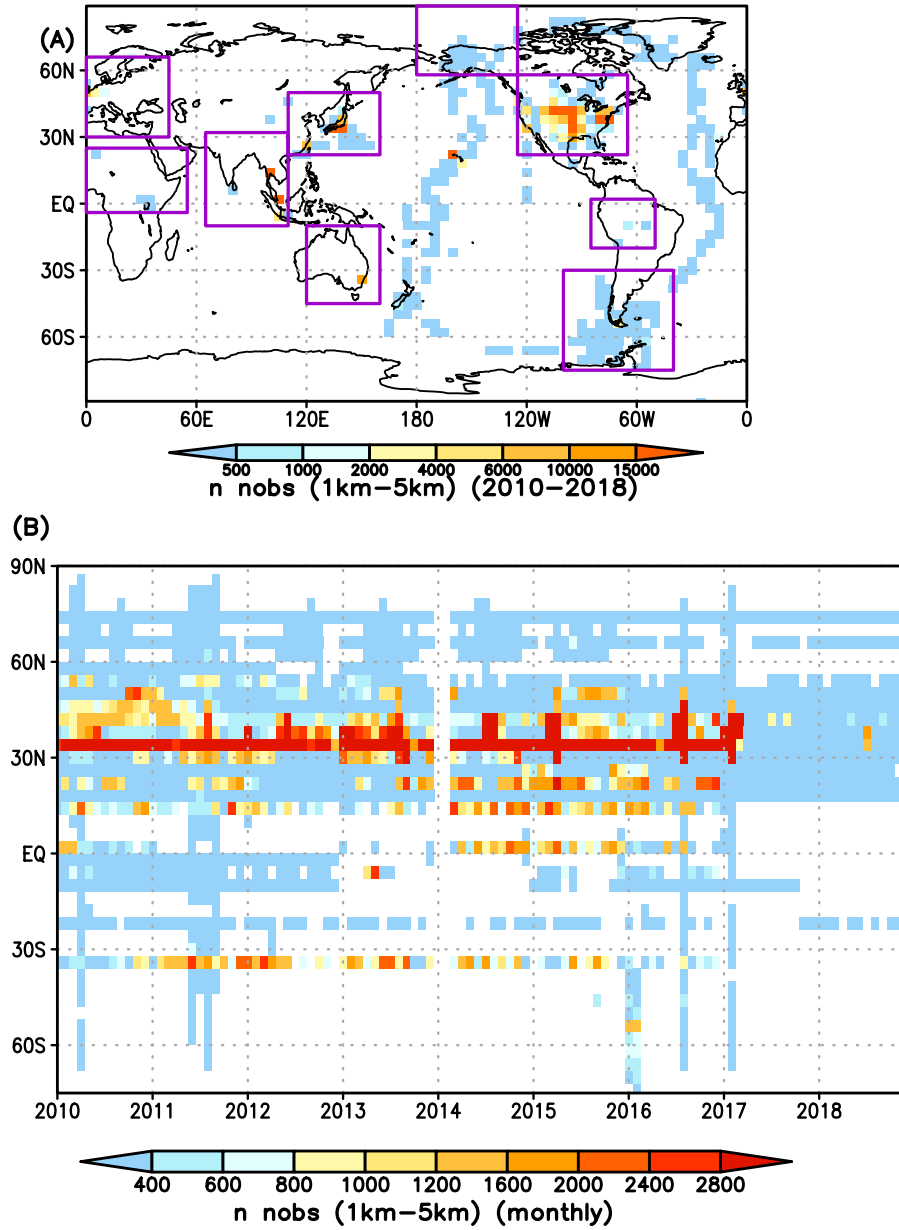
1227

1228

1229

1230

1231

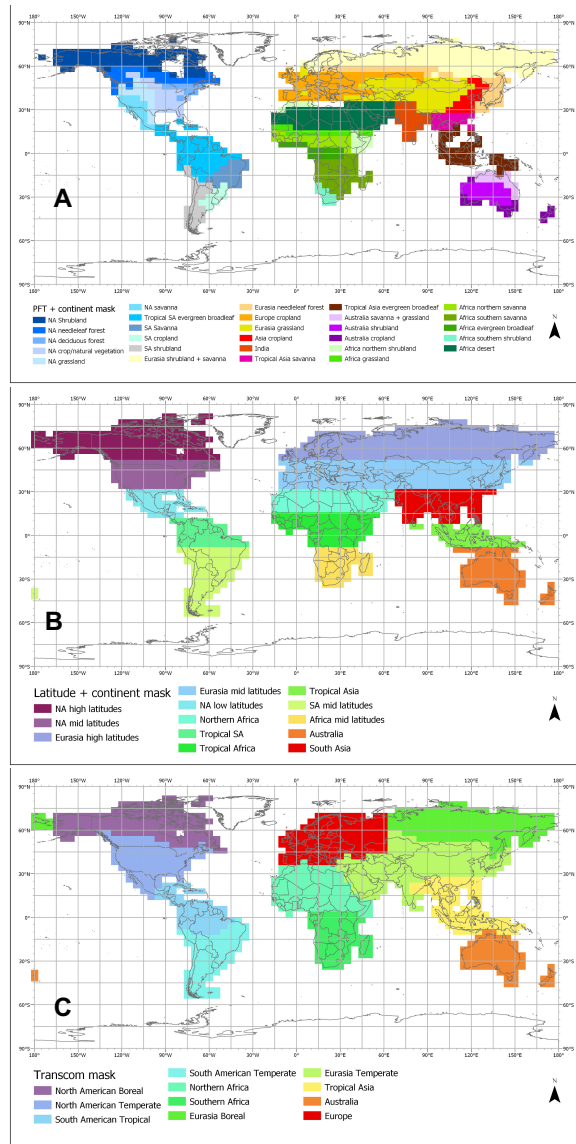


1232

1233 **Figure: 2 The spatial and temporal distributions of aircraft observations used in evaluation**
 1234 **of posterior NBE. (A) The total number of aircraft observations between 1–5 km between**
 1235 **2010–2018 at each 4° x 5° grid point. The rectangle boxes show the range of the nine sub**
 1236 **regions. (B) The total number of monthly aircraft observations at each longitude as a**
 1237 **function of time.**

1238

1239



1240

1241 **Figure: 3 Three types of regional masks used in calculating regional fluxes. A: the mask is**
 1242 **based on a combination of condensed seven MODIS IGBP plant functional types,**
 1243 **TRANCOM-3 regions (Gurney et al., 2004), and continents. B: the mask is based on latitude**
 1244 **and continents. C: the TransCom region mask.**

1245

1246

1247

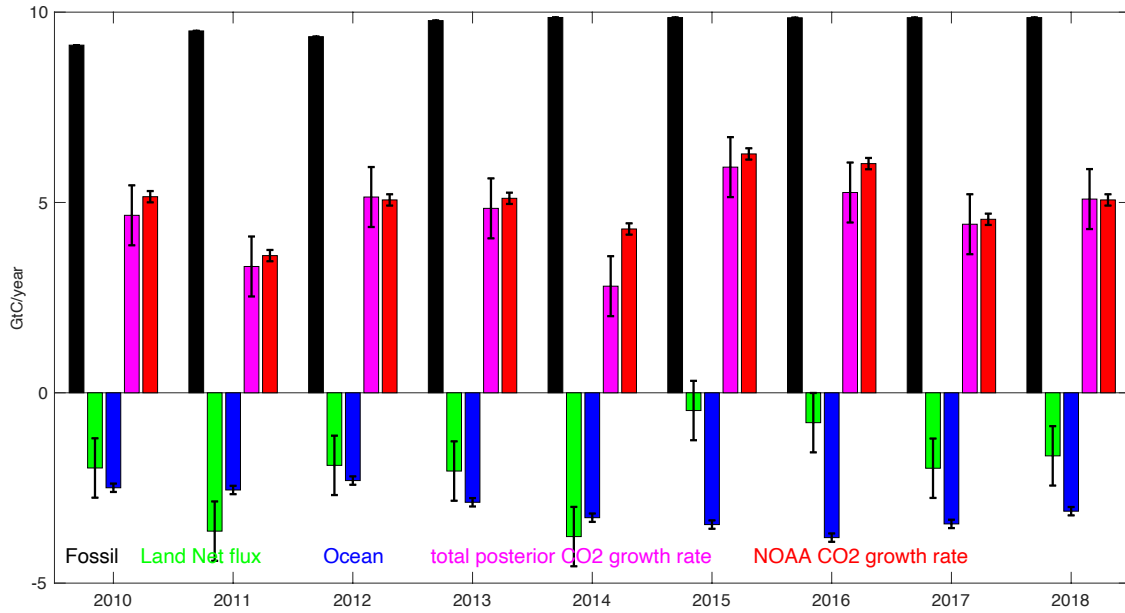
1248

1249

1250

1251

1252



1253

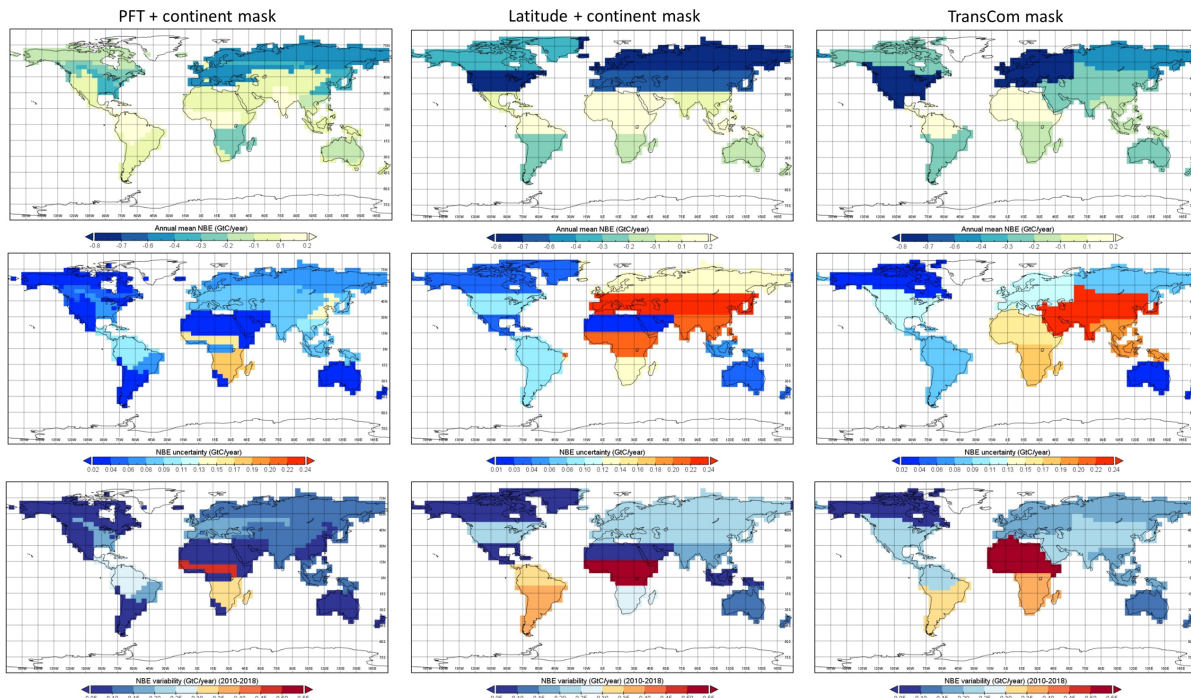
1254

1255

1256

1257

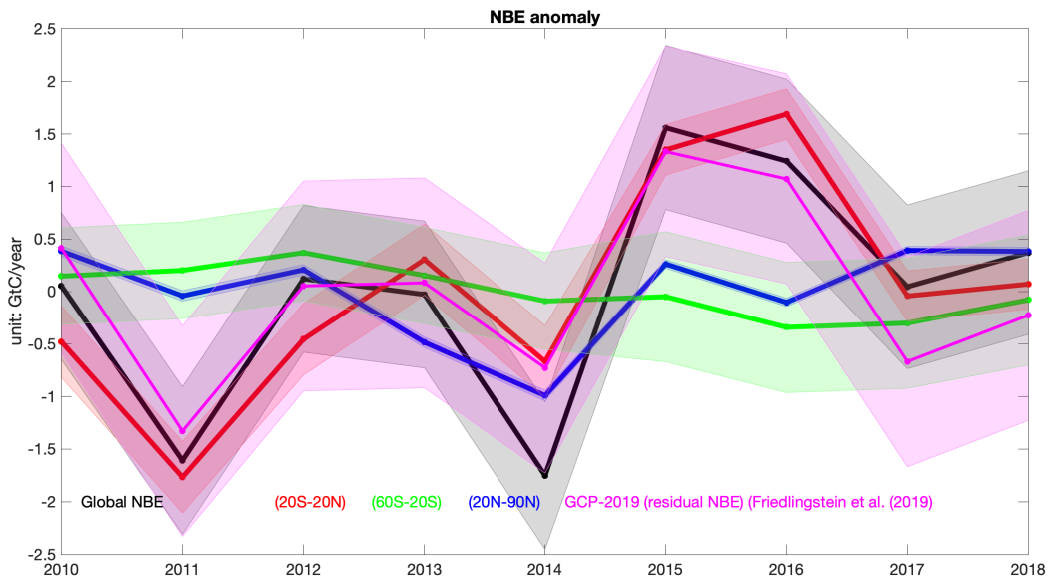
Figure: 4 Global flux estimation and uncertainties from 2010 –2018 (black: fossil fuel; green: posterior land fluxes; blue: ocean fluxes; magenta: estimated CO₂ growth rate; red: the NOAA CO₂ growth rate).



1259
 1260
 1261
 1262
 1263
 1264
 1265

Figure: 5 Mean annual regional NBE (A, B, and C), uncertainty (D, E, and F), and variability between 2010–2018 (G, H, and I) with the three types of regional masks (Figure 3). The first column uses a region mask based on PFT and continents (RM1). The second column uses a region mask based latitude and continents (RM2), and the third column uses TransCom mask.

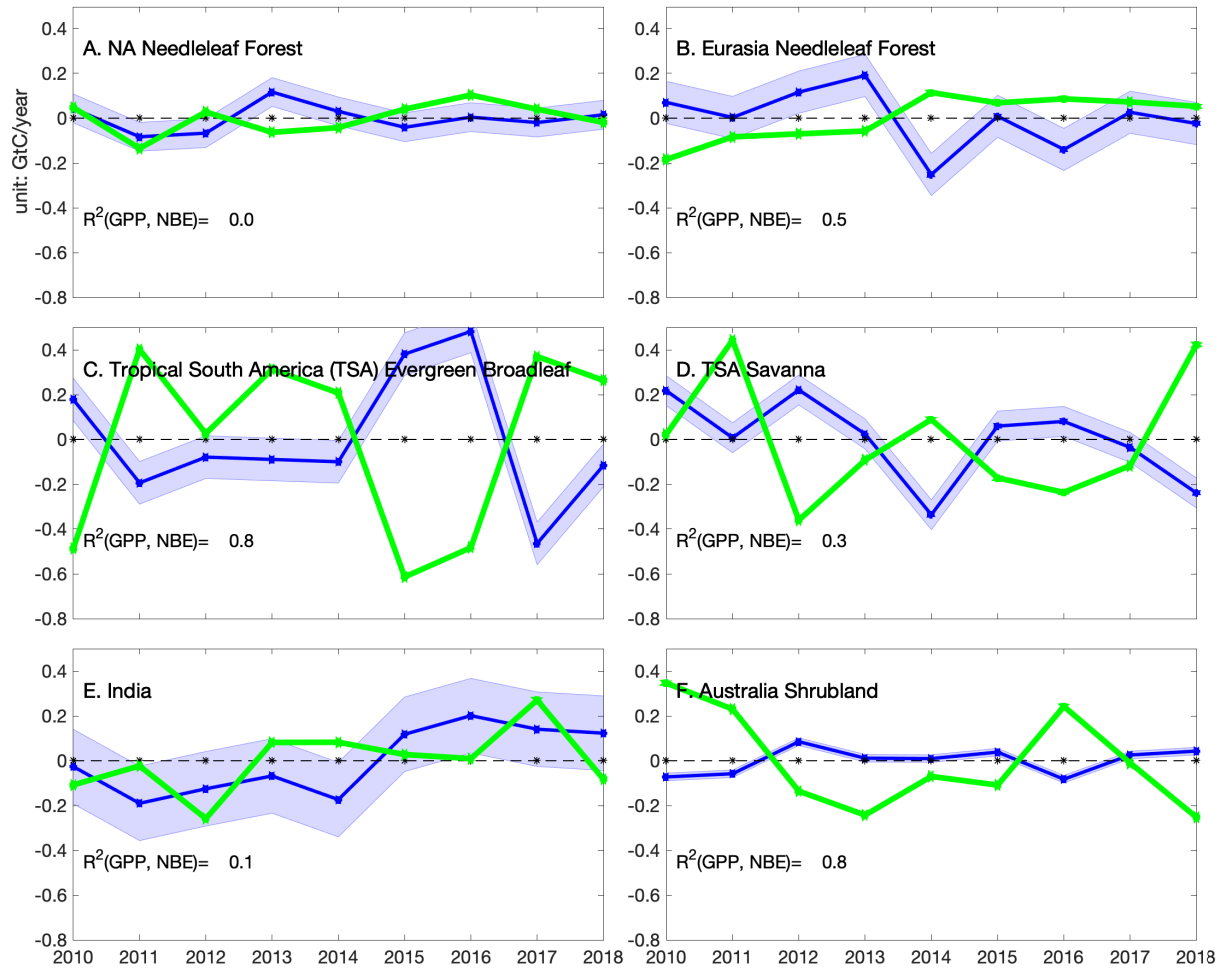
1266



1267

1268 **Figure: 6** The NBE interannual variability over the globe (black), the tropics (20°S–20°N),
1269 SH mid-latitudes (60°S–20°S), and NH mid-latitudes (20°N–9°0N). For reference, the
1270 residual net land carbon sink from GCB-2019 (Friedlingstein et al., 2019) and its uncertainty
1271 is also shown (magenta).

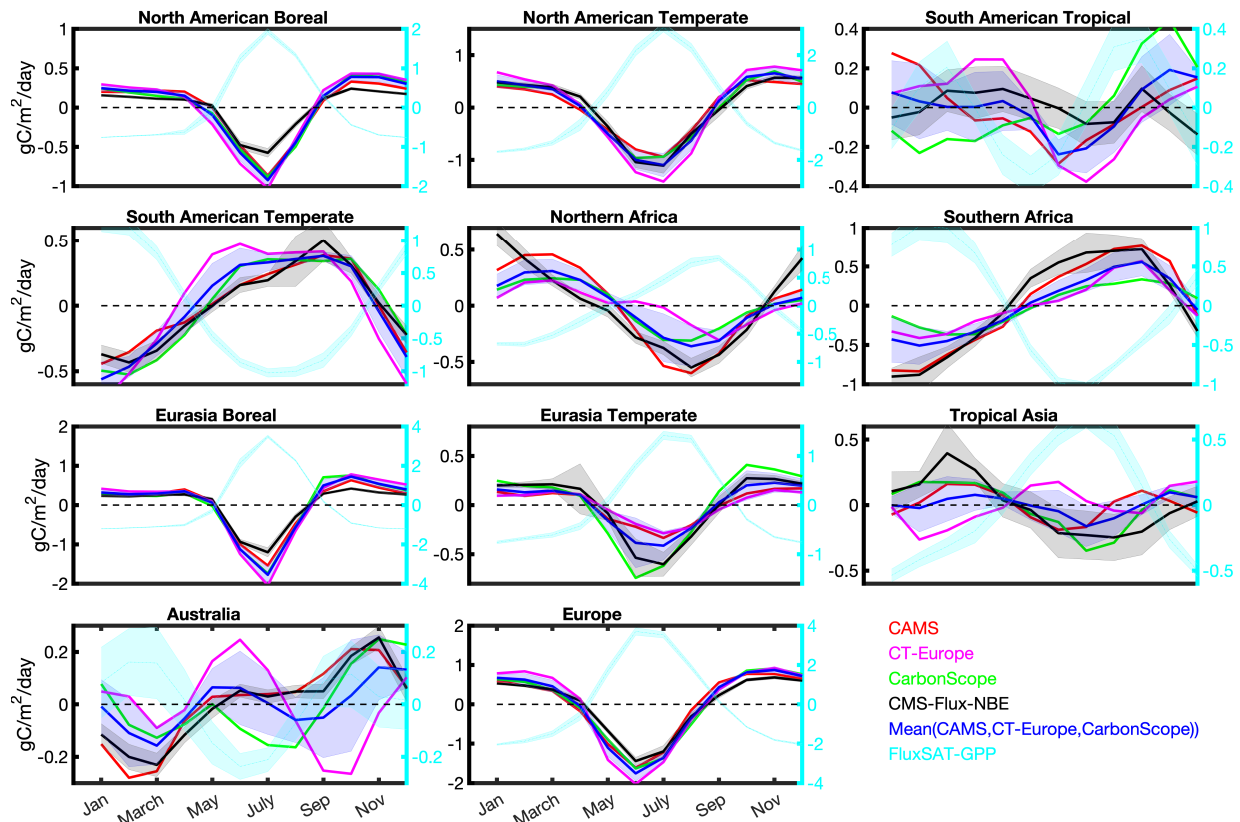
1272
1273
1274
1275



1276

1277
 1278
 1279
 1280
 1281
 1282

Figure: 7 The NBE interannual variability over six selected regions. Blue: annual NBE anomaly and its uncertainties. Green: annual GPP anomaly based on FLUXSAT.



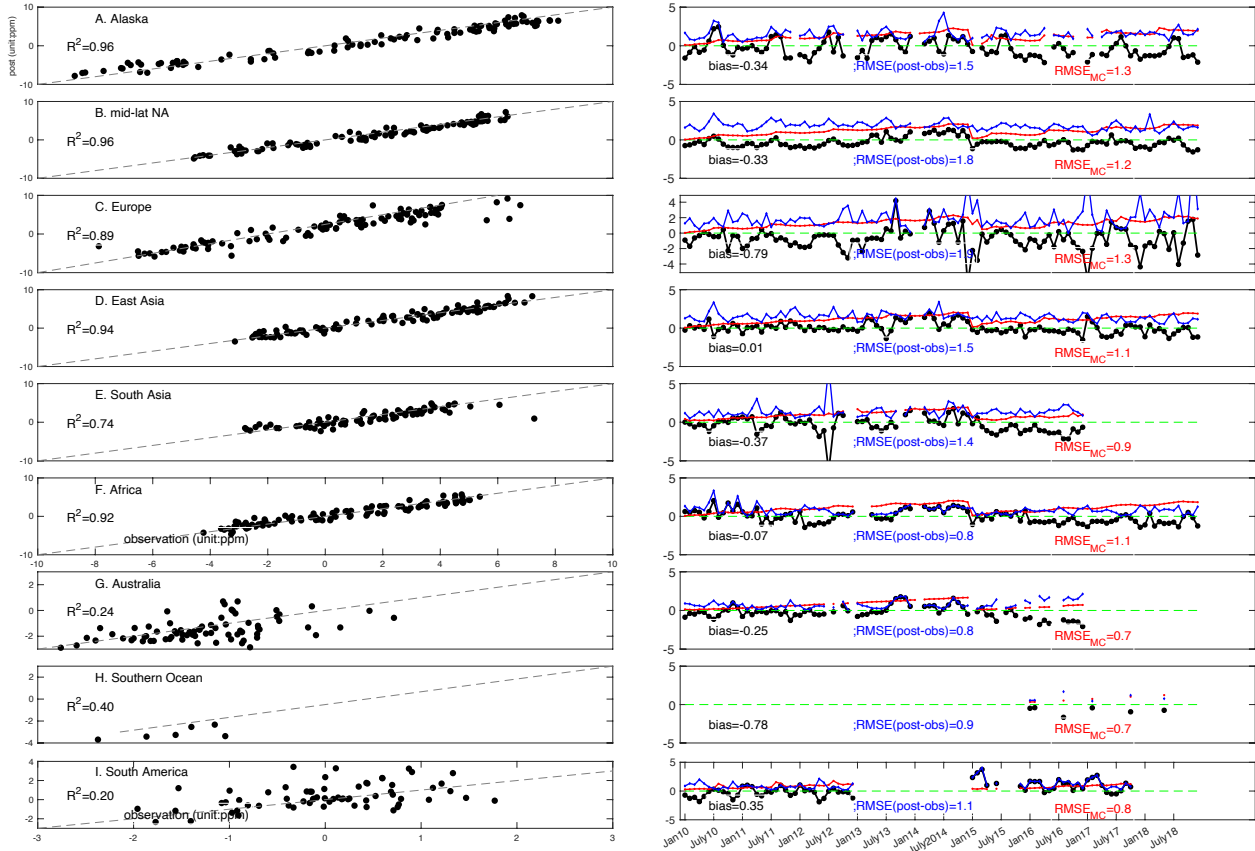
1283
 1284 **Figure: 8** The NBE climatological seasonality over TransCom regions. The seasonal cycle is
 1285 calculated over 2010-2017 since CT-Europe only covers till 2017. Black: CMS-Flux-NBE and
 1286 its uncertainty; blue shaded: mean NBE seasonality based on surface CO₂ inversion results
 1287 from CAMS, CT-Europe, and Jena CarbonScope; red: CAMS; magenta: CT-Europe; green:
 1288 Jena CarbonScope. The names of each region are shown on individual subplots.
 1289

1290

1291

1292

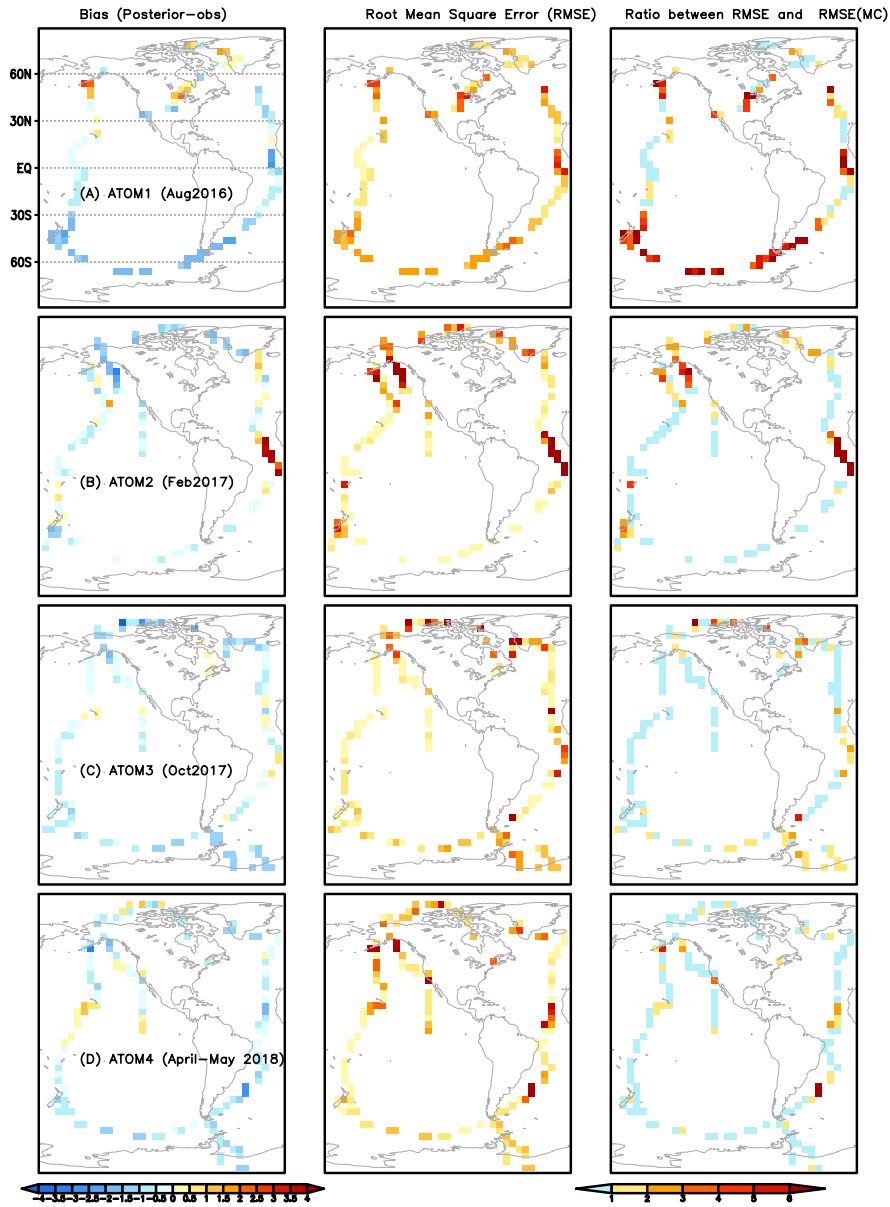
1293



1294

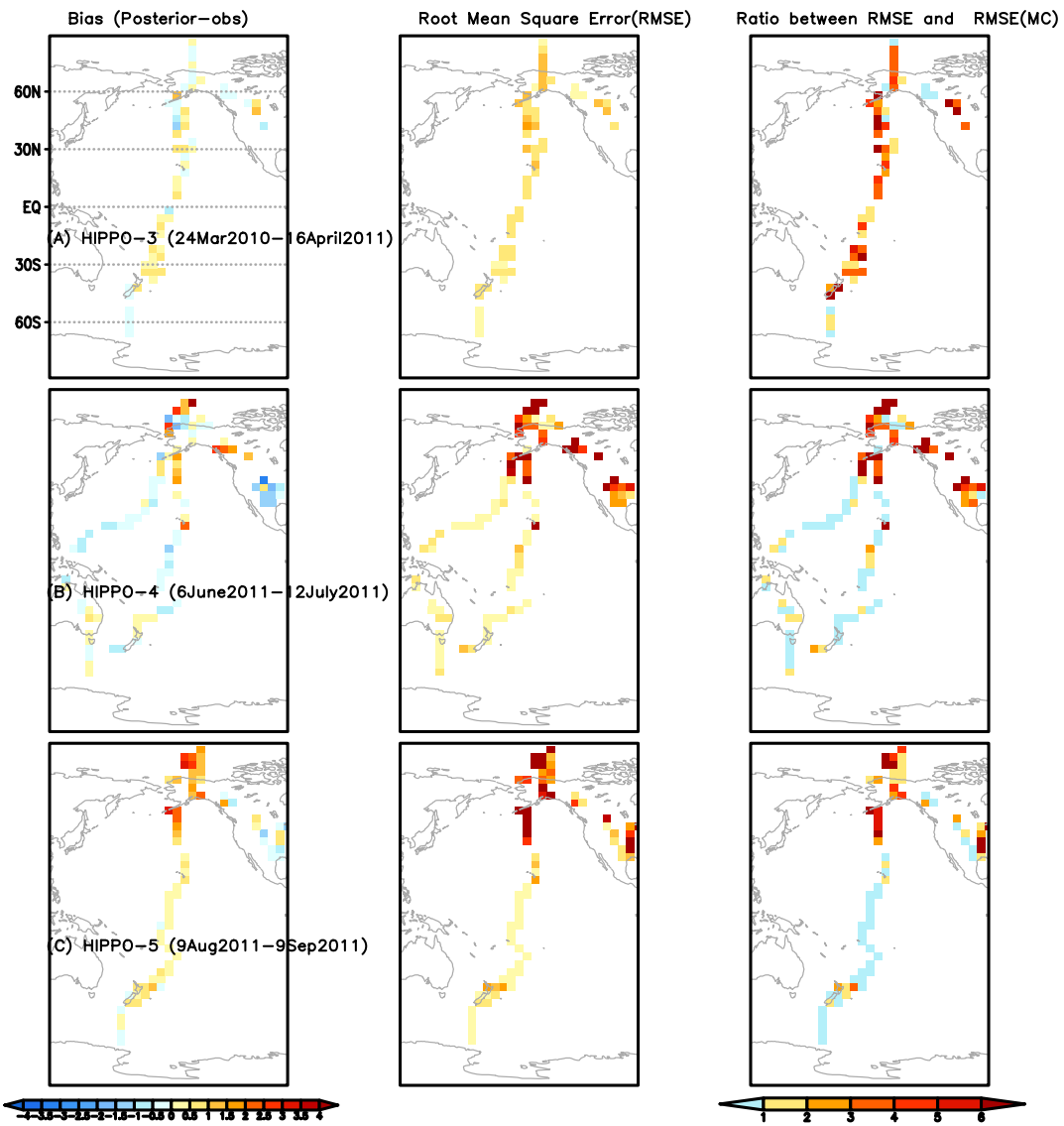
1295 **Figure: 9 Comparison between posterior CO₂ mole fraction and aircraft observations. Left**
 1296 **panel: detrended posterior CO₂ (y-axis) vs. detrended aircraft CO₂ (x-axis) over nine regions.**
 1297 **The dashed line is 1:1 line; right panel: black: the differences between posterior CO₂ and**
 1298 **aircraft CO₂ as a function of time; blue: RMSE (unit: ppm); red: RMSE_{MC}.**
 1299

1300
1301



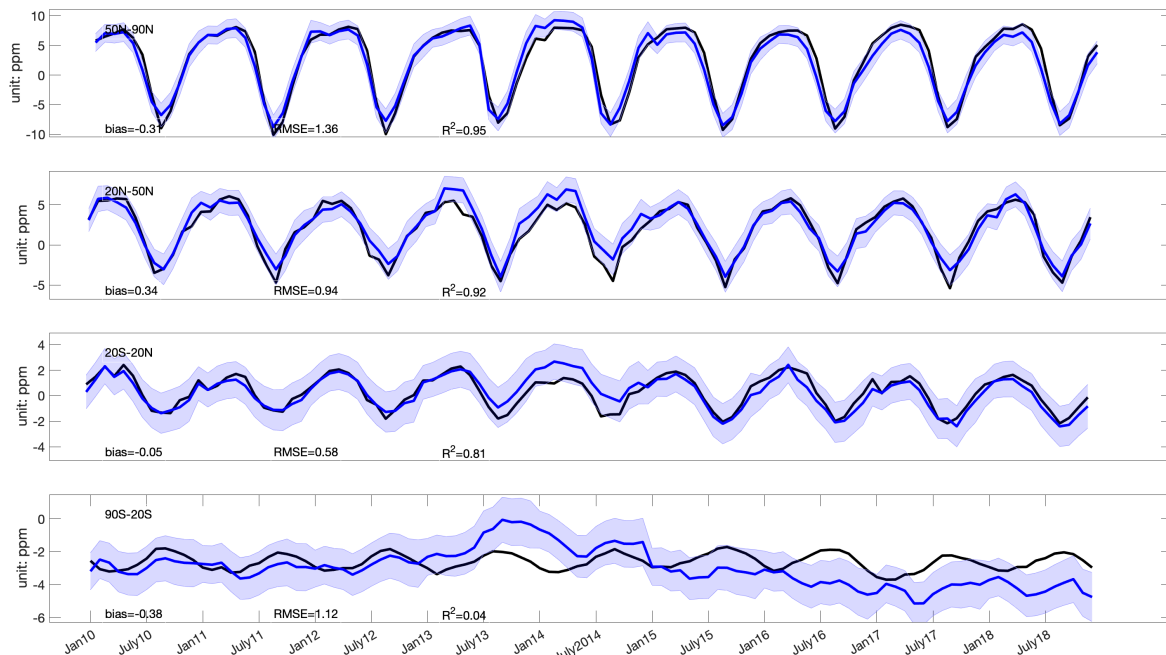
1302

1303 **Figure: 10** Left column: the mean differences between posterior CO₂ and aircraft
1304 observations from ATOM 1–4 aircraft campaigns between 1–5 km (A–D). Middle column:
1305 the Root Mean Square Errors (RMSE) between aircraft observations and posterior CO₂
1306 between 1–5 km. The color bar is the same as the left column. Right column: the ratio
1307 between RMSE and RMSE_{MC} based on ensemble CO₂ from the Monte Carlo uncertainty
1308 estimation method.



1309

1310 **Figure: 11** Left column: the mean differences between posterior CO₂ and aircraft
 1311 observations from HIPPO 3-5 aircraft campaigns between 1-5 km (A-C) (unit: ppm). (unit:
 1312 ppm). The time frame of each campaign is in the figure. Middle column: the Root Mean
 1313 Square Errors (RMSE) between aircraft observations and posterior CO₂ between 1-5 km
 1314 (unit: ppm). The color bar is the same as the left column. Right column: the ratio between
 1315 RMSE and RMSE_{MC} based on ensemble CO₂ from the Monte Carlo method.
 1316
 1317



1318
 1319 **Figure: 12 Comparison between posterior CO₂ and the NOAA marine boundary layer (MBL)**
 1320 **reference sites. Black: observations averaged over each latitude bands; blue and shaded area:**
 1321 **posterior CO₂ and its uncertainty. The global mean CO₂**
 1322 **(<https://www.esrl.noaa.gov/gmd/ccgg/trends/global.html>) was subtracted from both the**
 1323 **NOAA MBL reference and posterior CO₂ before the comparison.**
 1324

1325
 1326
 1327
 1328
 1329
 1330
 1331

Table: 1 Configurations of the CMS-Flux atmospheric inversion system

	Model setup	Configuration	Reference
Inversion general setup	Spatial scale	Global	--
	Spatial resolution	4° latitude x 5° longitude	
	Time resolution	monthly	
	Minimizer of cost function	L-BFGS	Byrd et al., 1994; Zhu et al., 1997
	Control vector	Monthly net terrestrial biosphere fluxes and ocean fluxes	
Transport model	Model name	GEOS-Chem and its adjoint	Suntharalingam et al., 2004 Nassar et al., 2010 Henze et al., 2007
	Meteorological forcing	GEOS-5 (2010–2014) and GEOS-FP (2015–2019)	Rienecker et al., 2008

1332
 1333

1334

1335 **Table: 2 Description of the prior fluxes and assumed uncertainties in the inversion system**

Prior fluxes	Terrestrial biosphere fluxes	Ocean fluxes	Fossil fuel emissions
Model name	CARDAMOM-v1	ECCO-Darwin	ODIAC 2018
Spatial resolution	4° x 5°	0.5°	1° x 1°
Frequency	3-hourly	3-hourly	hourly
Uncertainty	Estimated from CARDAMOM	100% same as Liu et al. (2017)	No uncertainty
References	Bloom et al., 2006; 2020	Brix et al, 2015; Carroll et al., 2020	Oda et al., 2016; 2018

1336

1337

1338

1339

1340

Table: 3 Description of observation and evaluation dataset. Data sources are listed in Table 7.

	Dataset name and version	References
Satellite X_{CO_2}	ACOS-GOSAT v7.3	O'Dell et al., (2012)
	OCO-2 v9	O'Dell et al., (2018)
Aircraft CO_2 observations	ObsPack OCO-2 MIP	CarbonTracker team (2019)
	HIPPO 3-5	Wofsy et al. (2011)
	ATom 1-4	Wofsy et al. (2018)
	INPE	Gatti et al., (2014)
	ORCAS	Stephens et al. (2017)
	ACT-America	Davis et al. (2018)
NOAA marine boundary layer (MBL) reference	NOAA MBL reference	Conway et al., 1994
GPP	FLUXSAT-GPP	Joiner et al., (2018)
Top-down NBE estimates constrained by surface CO_2	CarbonTracker-Europe	van der Laan-Luijkx et al. (2017) Peters et al., (2010) Peters et al. (2007)
	Jena CarbonScope s10oc v2020	Rödenbeck et al., 2003
	CAMS v18r1	Chevallier et al., 2005

1341

1342
1343
1344

Table: 4 Latitude and longitude ranges for seven sub regions.

Region	Alaska	Mid-lat NA	Europe	East Asia	South Asia
Longitude range	180°W–125° W	125°W–65°W	5°W–45°E	110°E–160°E	65°E–110°E
Latitude range	58°N–89°N	22°N–58°N	30°N–66°N	22°N–50°N	10°S–32°N
Region	Africa	South America	Australia	Southern Ocean	
Longitude range	5°W–55°E	95°W–50°W	120°E–160°E	110°W–40°E	
Latitude range	2°N–18°N	20°S–2°N	45°S–10°S	80°S–30°S	

1345
1346

1347 **Table: 5 List of the data products.**

Product	Spatial resolution	Temporal resolution when applicable	Data format	Sample data description in the text
Total fossil fuel, ocean, and land fluxes	Global	Annual	<i>csv</i>	Figure 4 (section 4.1)
Climatology mean NBE, variability, and uncertainties	PFT and continents based 28 regions	N/A	<i>csv</i>	Figure 5 (section 4.2)
	Geographic-based 13 regions		<i>csv</i>	
	TransCom regions		<i>csv</i>	
Hemispheric NBE and uncertainties	NH (20°N-90°N), tropics (20°S-20°N), and SH (60°S-20°S)	Annual	<i>csv</i>	Figure 6 (section 4.3)
NBE variability and uncertainties	PFT and continents based 28 regions	Annual	<i>csv</i>	Figure 7 (section 4.3)
	Geographic -based 13 regions		<i>csv</i>	
	TransCom regions		<i>csv</i>	
NBE seasonality and its uncertainties	PFT and continents based 28 regions	Monthly	<i>csv</i>	Figure 8 (section 4.4)
	Geographic -based 13 regions		<i>csv</i>	
	TransCom regions		<i>csv</i>	
Monthly NBE and uncertainties	PFT and continents based 28 regions	Monthly	<i>csv</i>	N/A
	Geographic -based 13 regions		<i>csv</i>	
	TransCom		<i>csv</i>	
Gridded posterior NBE, air-sea carbon exchanges, and uncertainties	4° (latitude) x 5° (longitude)	Monthly	<i>NetCDF</i>	N/A
Gridded prior NBE and air-sea carbon exchanges	4° (latitude) x 5° (longitude)	Monthly and 3-hourly	<i>NetCDF</i>	N/A
Gridded fossil fuel emissions	4° (latitude) x 5° (longitude)	Monthly mean and hourly	<i>NetCDF</i>	N/A
Region masks	PFT and continents based 28 regions	N/A	<i>csv</i>	Figure 3 (section 2.4)
	Geographic -based 13 regions			
	TransCom regions			

1348

1349

1350 **Table: 6 The nine-year mean regional annual fluxes, uncertainties, and variability. Regions**
 1351 **are based on the mask shown in Figure 5A (Figure 5.csv). Unit: GtC/year**

Region name (Figure4.csv)	Mean NBE	Uncertainty	Variability
NA shrubland	-0.14	0.02	0.05
NA needleleaf forest	-0.22	0.04	0.06
NA deciduous forest	-0.2	0.04	0.07
NA crop natural vegetation	-0.41	0.06	0.18
NA grassland	-0.04	0.03	0.03
NA savannah	0.03	0.02	0.03
Tropical South America (SA) evergreen broadleaf	0.04	0.1	0.28
SA savannah	-0.09	0.06	0.18
SA cropland	-0.07	0.03	0.07
SA shrubland	-0.03	0.02	0.08
Eurasia shrubland savanna	-0.44	0.07	0.14
Eurasia needleleaf forest	-0.41	0.07	0.12
Europe cropland	-0.46	0.09	0.16
Eurasia grassland	0.02	0.08	0.13
Asia cropland	-0.37	0.13	0.08
India	0.14	0.09	0.14
Tropical Asia savanna	-0.12	0.11	0.08
Tropical Asia evergreen broadleaf	-0.09	0.09	0.12
Australia (Aus) savannah grassland	-0.11	0.02	0.09
Aus shrubland	-0.07	0.01	0.05
Aus cropland	-0.01	0.01	0.03
African (Afr) northern shrubland	0.04	0.02	0.03
Afr grassland	0.03	0.01	0.01
Afr northern savanna	0.54	0.15	0.49
Afr southern savanna	-0.27	0.18	0.33
Afr evergreen broadleaf	0.1	0.07	0.09
Afr southern shrubland	0.01	0.01	0.01
Afr desert	0.06	0.01	0.04

1352

1353

1354 **Table: 7 Lists of data sources used in producing and evaluating posterior NBE product.**

Data name	Data Source
ECCO-Darwin ocean fluxes	https://doi.org/10.25966/4v02-c391
CARDAMOM NBE and uncertainties	https://doi.org/10.25966/4v02-c391
ODIAC	http://db.cger.nies.go.jp/dataset/ODIAC/DL_odiad2019.html
GOSAT b7.3	https://oco2.gesdisc.eosdis.nasa.gov/data/GOSAT_TANSO_Level2/ACOS_L2S.7.3/
OCO-2 b9	https://disc.gsfc.nasa.gov/datasets?page=1&keywords=OCO-2
ObsPack	https://www.esrl.noaa.gov/gmd/ccgg/obspack/data.php
ATom 1-4	https://daac.ornl.gov/ATOM/guides/ATom_merge.html
HIPPO 3-5	https://www.eol.ucar.edu/field_projects/hippo
INPE	https://www.esrl.noaa.gov/gmd/ccgg/obspace_co2_1_INPE_RESTRICTED_v2.0_2018-11-13 and
FLUXSAT-GPP	https://gs614-avdc1-pz.gsfc.nasa.gov/pub/tmp/FluxSat_GPP/
NOAA MBL reference	https://www.esrl.noaa.gov/gmd/ccgg/mb1/index.html
CarbonTracker-Europe NBE	https://www.carbontracker.eu/download.shtml
Jena CarbonScope NBE	http://www.bgc-jena.mpg.de/CarboScope/?ID=s
CAMS NBE	https://apps.ecmwf.int/datasets/data/cams-ghg-inversions/?date_month_slider=2009-12,2018-12&param=co2&datatype=ra&version=v17r1&frequency=mm&quantity=surface_flux
Posterior NBE	https://doi.org/10.25966/4v02-c391

1355

1356

1357

1358

1359